

1 **Regional pollen-based Holocene temperature and**
2 **precipitation patterns depart from the Northern Hemisphere**
3 **mean trends**

4 Ulrike Herzschuh^{1,2,3}, Thomas Böhmer¹, Manuel Chevalier^{4,5}, Raphaël Hébert¹, Anne
5 Dallmeyer⁶, Chenzhi Li^{1,2}, Xianyong Cao^{1,7}, Odile Peyron⁸, Larisa Nazarova^{1,9}, Elena Y.
6 Novenko^{10,11}, Jungjae Park^{12,13}, Natalia A. Rudaya^{14,15}, Frank Schlütz^{16,17}, Lyudmila S.
7 Shumilovskikh¹⁷, Pavel E. Tarasov¹⁸, Yongbo Wang¹⁹, Ruilin Wen^{20,21}, Qinghai Xu²², Zhuo
8 Zheng^{23,24}

9 ¹ Polar Terrestrial Environmental Systems, Alfred Wegener Institute Helmholtz Centre for Polar and
10 Marine Research, Telegrafenberg A45, 14473 Potsdam, Germany

11 ² Institute of Environmental Science and Geography, University of Potsdam, Karl-Liebkecht-Str. 24–25,
12 14476 Potsdam, Germany

13 ³ Institute of Biochemistry and Biology, University of Potsdam, Karl-Liebkecht-Str. 24–25, 14476
14 Potsdam, Germany

15 ⁴ Institute of Geosciences, Sect. Meteorology, Rheinische Friedrich-Wilhelms-Universität Bonn, Auf dem
16 Hügel 20, 53121 Bonn, Germany

17 ⁵ Institute of Earth Surface Dynamics IDYST, Faculté des Géosciences et l'Environnement, University
18 of Lausanne, Bâtiment Géopolis, 1015 Lausanne, Switzerland

19 ⁶ Max Planck Institute for Meteorology, Bundesstraße 53, 20146 Hamburg, Germany

20 ⁷ Alpine Paleoecology and Human Adaptation Group (ALPHA), State Key Laboratory of Tibetan Plateau
21 Earth System, Resources and Environment (TPESRE), Institute of Tibetan Plateau Research, Chinese
22 Academy of Sciences, 100101 Beijing, China

23 ⁸ Institut des Sciences de l'Evolution de Montpellier, Université de Montpellier, CNRS UMR 5554,
24 Montpellier, France

25 ⁹ Institute of Geology and Petroleum Technologies, Kazan Federal University, Kremlyovskaya Street 18,
26 420008 Kazan, Russia

27 ¹⁰ Faculty of Geography, Lomonosov Moscow State University, Leniskie Gory 1, 119991 Moscow,
28 Russia

29 ¹¹ Department of Quaternary Paleogeography, Institute of Geography Russian Academy of Science,
30 Staromonrtny Lane 29, 119017 Moscow, Russia

31 ¹² Department of Geography, Seoul National University, 1 Gwanak-ro, Gwanak-gu, Seoul 08826,
32 Republic of Korea

33 ¹³ Institute for Korean Regional Studies, Seoul National University, 1 Gwanak-ro, Gwanak-gu, Seoul
34 08826, Republic of Korea

35 ¹⁴ PaleoData Lab, Institute of Archaeology and Ethnography, Siberian Branch, Russian Academy of
36 Sciences, Pr. Akademika 36 Lavrentieva 17, 630090 Novosibirsk, Russia

37 ¹⁵ Biological Institute, Tomsk State University, Pr. Lenina, 26, 634050 Tomsk, Russia

38 ¹⁶ Institute for Pre- and Protohistoric Archaeology, University of Kiel, Germany, Johanna-Mestorf-Straße
39 2–6, 24118 Kiel, Germany

40 ¹⁷ Department of Palynology and Climate Dynamics, Georg-August-University of Göttingen, Wilhelm
41 Weber Str. 2a, 37073 Göttingen, Germany

42 ¹⁸ Institute of Geological Sciences, Palaeontology Section, Freie Universität Berlin, Malteserstraße 74–
43 100, Building D, 12249 Berlin, Germany

44 ¹⁹ College of Resource Environment and Tourism, Capital Normal University, 105 West Third Ring Road
45 North, 100048 Beijing, China

46 ²⁰ Key Laboratory of Cenozoic Geology and Environment, Institute of Geology and Geophysics, Chinese
47 Academy of Sciences, 19 Beitucheng West Road, Chaoyang District, 100029 Beijing, China

48 ²¹ Center for Excellence in Life and Paleoenvironment, Chinese Academy of Sciences, 100044 Beijing,
49 China

50 ²² School of Geographic Sciences, Hebei Normal University, 050024 Shijiazhuang, China

51 ²³ Guangdong Key Lab of Geodynamics and Geohazards, School of Earth Sciences and Engineering,
52 Sun Yat-sen University, 519082 Zhuhai, China

53 ²⁴ Southern Marine Science and Engineering Guangdong Laboratory (Zhuhai), 519082 Zhuhai, China

54 *Correspondence to:* Ulrike Herzs Schuh (Ulrike.Herzs Schuh@awi.de)

55

56 **Abstract.** A mismatch between model- and proxy-based Holocene climate change, known as the
57 ‘Holocene conundrum’, may partially originate from the poor spatial coverage of climate reconstructions
58 in, for example, Asia, limiting the number of grid cells for model-data comparisons. Here we investigate
59 hemispheric, latitudinal, and regional mean time-series as well as time-slice anomaly maps of pollen-
60 based reconstructions of mean annual temperature, mean July temperature, and annual precipitation
61 from 1908 records in the Northern Hemisphere extratropics. Temperature trends show strong latitudinal
62 patterns and differ between (sub-)continents. While the circum-Atlantic regions in Europe and Eastern
63 North America show a pronounced Mid-Holocene temperature maximum, Western North America
64 shows only weak changes and Asia mostly shows a continuous Holocene temperature increase.
65 Likewise, precipitation trends show certain regional peculiarities such as the pronounced Mid-Holocene
66 precipitation maximum between 40 and 50°N in Asia and Holocene increasing trends in Europe and

67 Western North America, which can all be linked with Holocene changes of the regional circulation pattern
68 responding to temperature change. Given a background of strong regional heterogeneity, we conclude
69 that the calculation of global or hemispheric means, which initiated the ‘Holocene conundrum’ debate,
70 should focus more on understanding the spatio-temporal patterns and their regional drivers.

71

72 **1 Introduction**

73 Previous comparisons of proxy-based reconstructions and simulations of global Holocene climate
74 change have yielded major mismatches, a discrepancy termed the ‘Holocene conundrum’ (Liu et al.,
75 2014c; Kaufman and Broadman, 2023). While simulations indicate an increase in Holocene temperature
76 (Liu et al., 2014c), proxy data syntheses rather support a Mid-Holocene temperature maximum (Marcott
77 et al., 2013; Kaufman et al., 2020b). Recently, several explanations for this finding were proposed, most
78 of which assign the mismatch to biases in the proxy data with respect to location or seasonality (Marsicek
79 et al., 2018; Bader et al., 2020; Bova et al., 2021; Osman et al., 2021).

80 Previous temperature reconstructions from continental areas are mainly available from the circum-North
81 Atlantic region, and are potentially unrepresentative of the whole Northern Hemisphere temperature
82 change, as the region was strongly impacted by the vanishing Laurentide ice-sheet (Rolandone et al.,
83 2003; Chouinard and Mareschal, 2009). Synthesis studies hitherto included rather few records from the
84 large non-glaciated Asian continent (Andreev et al., 2004; Leipe et al., 2015; Melles et al., 2012;
85 Nakagawa et al., 2002; Stebich et al., 2015; Tarasov et al., 2009 and 2013). The inclusion of recently
86 compiled Holocene pollen records (Cao et al., 2019; Herzschuh et al., 2019) and high-quality modern
87 pollen datasets (Tarasov et al., 2011; Cao et al., 2014; Davis et al., 2020; Dugerdil et al., 2021) from
88 Asia now allows for higher quality quantitative reconstructions.

89 While temperature patterns have often been studied, hemispheric syntheses of quantitative precipitation
90 change during the Holocene are not yet available. A recent study of qualitative moisture proxy data
91 suggests an overall warm and dry Mid-Holocene in the Northern Hemisphere mid-latitudes, related to
92 the weakened latitudinal temperature gradient (Routson et al., 2019). This trend contrasts with the idea
93 of positive hydrological sensitivity, that is, warm climates are wet at a global scale (Trenberth, 2011),
94 which was confirmed from proxy and model studies from monsoonal areas in lower latitudes (Kutzbach,
95 1981; Wang et al., 2017). However, the study of Routson et al. (2019) only included a few records from
96 the subtropical monsoonal Asia that is known for complex Holocene moisture patterns (Herzschuh, 2004;
97 Chen et al., 2019; Herzschuh et al., 2019). These and further synthesis studies (Wang et al., 2010; Chen
98 et al., 2015; Wang et al., 2020) also gave a plethora of alternative explanations to characterize these
99 patterns, including interactions between the monsoon and westerlies circulation and evaporation effects.

100 Pollen spectra are a well-established paleoclimate proxy and quantitative estimates of past climatic
101 change are mainly derived by applying (transfer functions of) modern pollen-climate calibration sets to
102 fossil pollen records (Birks et al., 2010; Chevalier et al., 2020). Accordingly, pollen-based
103 reconstructions constitute a substantial part of multi-proxy syntheses (e.g., Kaufman et al., 2020b), albeit
104 derived from different calibration sets and methods, which makes a consistent assessment of inherent

105 reconstruction biases difficult. Pollen data are one of the few land-derived proxies available that can
106 theoretically contain independent information on both temperature and precipitation in the same record
107 (Chevalier et al., 2020; Mauri et al., 2015). Consistent pollen-based reconstructions can thus contribute
108 to better characterizing past temperature and precipitation changes across large landmasses and how
109 these changes co-vary over time (Davis et al., 2003).

110 Here, we analyze spatio-temporal patterns of pollen-based reconstructions of mean annual temperature
111 (T_{ann}), mean July temperature (T_{July}), and mean annual precipitation (P_{ann}) from 1908 sites from the
112 Northern Hemisphere extratropics that were generated using harmonized methods and calibration
113 datasets (LegacyClimate 1.0, Herzschuh et al., 2022a) and have revised chronologies (Li et al., 2022).
114 We address the following questions: (1) What are the continental, latitudinal, and regional patterns of
115 Holocene temperature change in the Northern Hemisphere extratropics and how do our new
116 reconstructions align with the global averaged trends of a previous global temperature synthesis? (2)
117 What are the continental, latitudinal, and regional patterns of Holocene precipitation change and how
118 do these changes co-vary with temperature trends?

119

120 **2 Methods**

121 This study analyzes pollen-based reconstructions provided in the LegacyClimate 1.0 dataset
122 (Herzschuh et al., 2023). It contains pollen-based reconstructions of T_{July} , T_{ann} , and P_{ann} of 2593 records
123 along with transfer function metadata and estimates of reconstruction errors and is accompanied by a
124 manuscript analyzing reconstruction biases and presenting reliability tests (Herzschuh et al., 2022a).
125 The fossil pollen records, representing the LegacyPollen 1.0 dataset, were derived from multiple natural
126 archives, most commonly continuous lacustrine and peat accumulations (Herzschuh et al., 2022b), and
127 originate from the Neotoma Paleoecology Database ('Neotoma' hereafter; last access: April 2021;
128 Williams et al., 2018), a dataset from Eastern and Central Asia (Cao et al., 2013; Herzschuh et al., 2019),
129 a dataset from Northern Asia (Cao et al., 2019), and a few additional records to fill up some spatial data
130 gaps in Siberia.

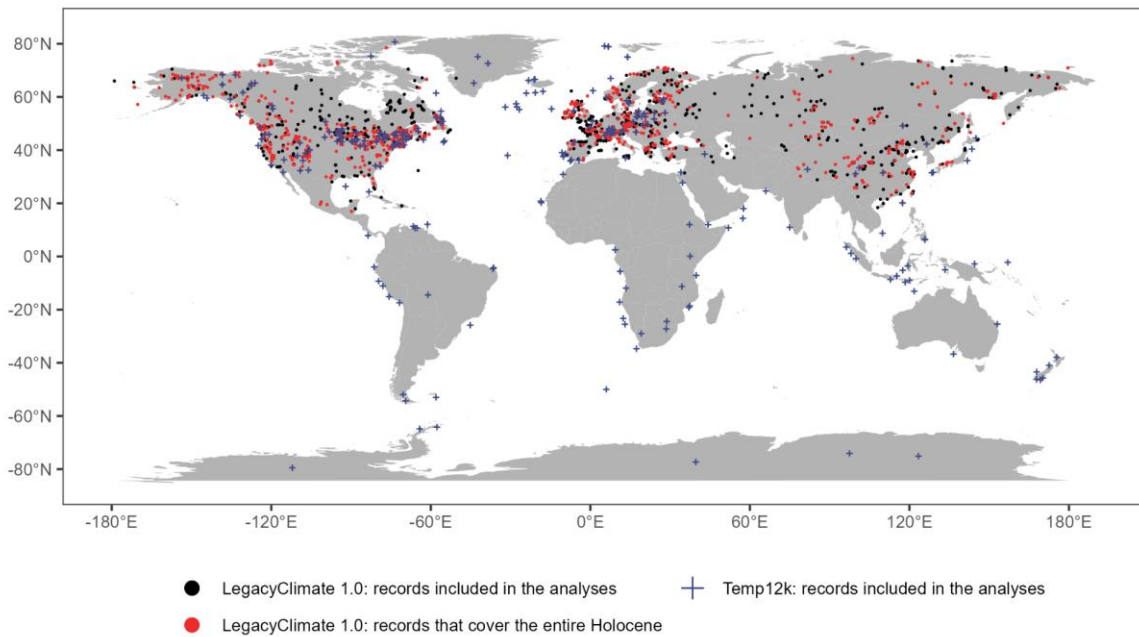
131 The chronologies of LegacyPollen 1.0 are based on revised 'Bacon' (Blaauw and Christen, 2011) age-
132 depth models with calibrated ages at each depth provided by Li et al. (2022). Taxa are harmonized to
133 genus level for woody and major herbaceous taxa and to family level for other herbaceous taxa. Along
134 with LegacyClimate 1.0, a taxonomically harmonized modern pollen dataset is provided (a total of 15379
135 samples; Herzschuh et al., 2022a) which includes datasets from Europe (EMPD2, Davis et al., 2020),
136 Asia (Tarasov et al., 2011; Herzschuh et al., 2019; Dugerdil et al., 2021), and North America (from
137 Neotoma; Whitmore et al., 2005). LegacyClimate 1.0 also provides the climate data for the sites of the
138 modern pollen samples that were derived from WorldClim 2 (Fick and Hijmans, 2017).

139 LegacyClimate 1.0 provides reconstructions based on different methodologies including two versions of
140 WA-PLS (weighted averaging partial least squares regression, a transfer function-based approach) and
141 MAT (modern analogue technique). For each fossil site, we calculated the geographic distance between
142 each modern sampling site and each fossil location and selected a unique calibration set from modern

143 sites within a 2000 km radius (Cao et al., 2014), as it was shown to be a good trade-off between analog
144 quality and quantity (Cao et al., 2017). For WA-PLS, the used component, typically first or second, was
145 identified using model statistics as derived from leave-one-out cross-validation based on the criterion
146 that an additional component be used only if it improves the root mean squared error (RMSE) by at least
147 5% (ter Braak and Juggins, 1993). A WA-PLS_tailored reconstruction is also provided in the
148 LegacyClimate 1.0 dataset (Herzschuh et al., 2022a), which addresses the problem that co-variation in
149 modern temperature and precipitation data can be transferred into the reconstruction. To reduce the
150 influence of one climate variable on the target variable, the modern range of the non-target variable is
151 reduced by tailoring the modern pollen dataset to a selection of sites with little covariance between the
152 two variables. For example, to reconstruct T_{July} we identified the P_{ann} range reconstructed by WA-PLS
153 and extended it by 25% at both ends. For the selection of sites in the modern training dataset, we then
154 restricted modern P_{ann} to that range accordingly. As such, we keep all information for reconstruction
155 from those modern pollen spectra that cover a wide temperature range but downweight the information
156 from pollen spectra covering a wide precipitation range. However, initial assessments did not show any
157 major differences compared to using the standard WA-PLS-derived reconstruction. Therefore, we do
158 not make use of this dataset for this study so as to be consistent with previous studies. For comparison,
159 we provide a plot with hemispheric, continental, and latitudinal mean curves for T_{July} , T_{ann} , and P_{ann}
160 reconstructed by WA-PLS_tailored in the supplement. The MAT reconstructions were derived from the
161 seven best analogs that we identified based on the dissimilarity measures between the fossil samples
162 and the modern pollen assemblages using the squared-chord distance metric (Simpson, 2012). MAT
163 reconstructions were highly correlated with those obtained by WA-PLS (Herzschuh et al., 2022a). Here,
164 we opted for the widely used WA-PLS, as it is less sensitive to the size and environmental gradient
165 length of the modern pollen dataset and is thus less affected by spatial autocorrelation effects and can
166 better handle poor analog situations (ter Braak and Juggins, 1993; Telford and Birks, 2011; Cao et al.,
167 2014; Chevalier et al., 2020). Statistical significance tests sensu Telford & Birks (2011) were performed
168 for each site for WA-PLS, WA-PLS_tailored and MAT and assessed in Herzschuh et al. (2022a).

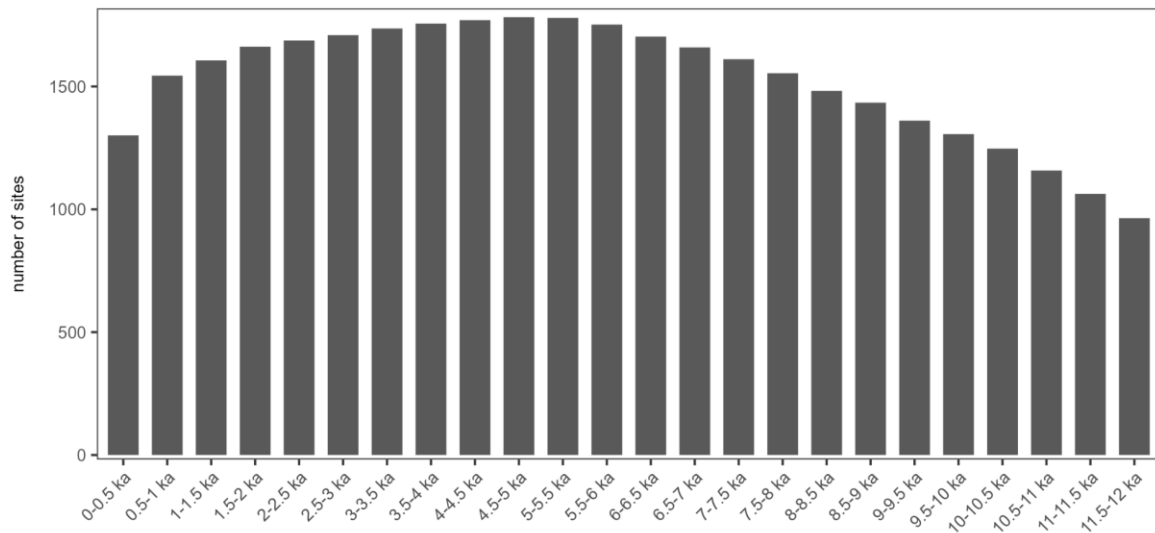
169 Of the 2593 records available in LegacyClimate 1.0, 1908 records with at least 5 samples that cover at
170 least 4000 years of the Holocene and have a mean temporal resolution of 1000 years or less were
171 included in the time-slice comparisons based on this criterion (Fig. 1). The construction of time-series
172 to estimate the means of climate variables was further restricted to 957 records that cover the full period
173 of 11 to 1 ka.

LegacyClimate 1.0 and Temp12k datasets | overview



174

Legacy Climate 1.0: number of records that cover a distinct time period



175

176 **Figure 1. (top) Spatial coverage of the LegacyClimate 1.0 (dots) and Temp12k (Kaufman et al.**
 177 **2020b, crosses) datasets used in this analysis.** The map shows sites that cover the entire Holocene
 178 (i.e., 11-1 ka) as red symbols and those that cover parts of the Holocene but at least 4000 years in the
 179 period between 12 and 0 ka as black symbols. (bottom) Temporal coverage of the LegacyClimate 1.0
 180 dataset.

181

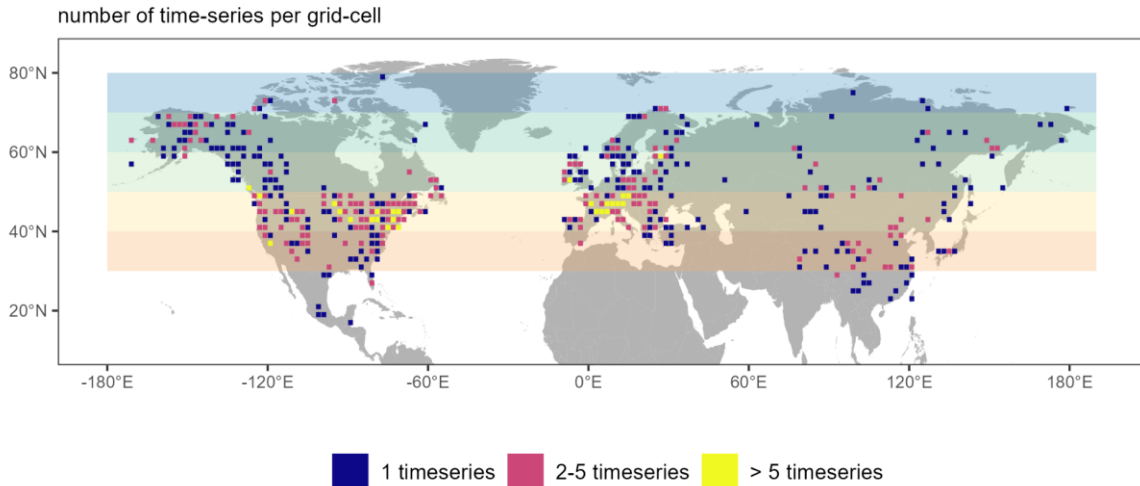
182 The mean root mean squared error of prediction (RMSEP; WA-PLS) from all 957 sites included in the
 183 time-series analyses is $2.4 \pm 0.7^\circ\text{C}$ (one standard deviation) for T_{July} , $2.6 \pm 0.5^\circ\text{C}$ for T_{ann} , and 244 ± 74 mm
 184 for P_{ann} . They show a spatial pattern in that the RMSEPs are higher in areas with steep climate gradients
 185 (e.g. Central Asia and along the western coast of North America; see Fig. 5 in Herzsuh et al., 2022a).

186 As it has already been shown in previous comparisons, WA-PLS can have higher RMSEPs than MAT
187 but these do not necessarily reflect a less reliable reconstruction but methodological differences. MAT
188 is known to be more sensitive to spatial autocorrelation, which causes the model performance to be
189 over-optimistic compared to WA-PLS (Cao et al., 2014). Besides, trends and the relative changes, as
190 interpreted in this study, are less sensitive to methodological biases than absolute values.

191 Derived time-series of T_{July} , T_{ann} , and P_{ann} were smoothed over a 500-yr time-scale and resampled at a
192 100 yr-resolution using the *corit* package in R (version 0.0.0.9000, Reschke et al., 2019). Because the
193 original time-series are unevenly spaced, we used this package as it is designed to resample irregularly
194 sampled time-series to an equidistant spacing (Reschke et al., 2019). The smoothing length of 500
195 years reflects the typical resolution of the original pollen records. These derived time-series were
196 sampled at selected time-slices and converted into a regular $2^\circ \times 2^\circ$ raster grid (by taking the mean of
197 all records located within the grid cell) using the *raster* package in R (version 3.5-11, R Core Team,
198 2020; Hijmans et al., 2021).

199 To calculate zonal, (sub-)continental (i.e., Asia ($>43^\circ\text{E}$), Europe ($<43^\circ\text{E}$), Eastern North America
200 ($<104^\circ\text{W}$; Williams et al., 2000) and Western North America), and hemispheric means we selected all
201 957 smoothed and resampled time-series of T_{July} , T_{ann} , and P_{ann} that cover the full period between 11
202 and 1 ka and calculated climate anomalies for all three climate variables. Rather than using the
203 anomalies for P_{ann} we calculated the precipitation change as % relative to the 1 ka reference period (Fig.
204 3) or relative to the younger time-slice (Fig. 4). The estimate at 1 ka was used as a reference to calculate
205 the anomalies, as many records either poorly or do not cover the last 0.5 ka. Weights proportional to the
206 inverse number of time-series per cell in the grid were used to calculate the weighted mean and standard
207 deviation (using the *wtd.mean* and *wtd.var* functions from the *Hmisc* R-package, version 5.0-1, Harrell
208 & Dupont, 2023). The weighted standard error was calculated by dividing the weighted standard
209 deviation estimates by the square root of the number of grid cells with at least 1 record. In total, 436 grid
210 cells between 17°N and 79°N are covered by one or more time-series (Fig. 2).

211 The zonal mean over 10° bands of (sub-)continents (e.g. for $30\text{-}40^\circ\text{N}$ of Europe) were calculated and
212 also used to calculate the mean time-series of the (sub-)continents, with weights proportional to the
213 terrestrial area in a zonal band based on the WGS84 EASE-Grid 2.0 global projection (Brodzik et al.,
214 2012). Likewise, the area-weighting was applied to derive the continental means and hemispheric-wide
215 (zonal) means. We compare the linear trends of all zonal means with each other for each continent, as
216 well as the linear trends of the continental weighted means, taking into account the standard error of
217 each average. We take a Monte-Carlo approach to generate ensembles of trend estimates after adding
218 random errors and use a standard t-test to assess, pairwise, whether the means of the ensembles are
219 significantly different.



220

221 **Figure 2. Number of time-series per grid cell.** The map shows the number of time-series that are
 222 merged into one grid cell. Colored rectangles (as used for the zonal mean curves in Fig. 3) indicate the
 223 latitudinal band a respective grid cell belongs to.

224

225 Furthermore, we extracted 325 records that cover the full Holocene period in the Temp12k dataset
 226 (version 1-1-0; <https://lipdverse.org/project/temp12k>, last access February 2023; Kaufman et al., 2020b)
 227 applying the same restrictions as with the LegacyClimate 1.0 dataset (i.e., at least 5 samples, a mean
 228 temporal resolution of 1000 years or less). Instead of 11.0 ka we here used a cut-off of 10.5 ka as many
 229 records in this dataset start shortly after 11.0 ka). For 43 sites, more than one temperature time-series
 230 were stored in the Temp12k dataset. In these cases, we selected that time-series with the least amount
 231 of missing temperature values in the period between 10.5 and 1 ka, leaving 272 records that were used
 232 to construct the mean temperature anomaly time-series similar to the approach described for the
 233 LegacyClimate 1.0 dataset. We excluded all pollen-based reconstructions from the Temp12k dataset
 234 between 30°N and 80°N (n=117) to avoid duplications with the LegacyClimate 1.0 dataset when
 235 integrating both datasets into a joint hemispheric and global mean temperature stack curve.

236

237 3 Results

238 3.1 Spatio-temporal pattern of temperature reconstructions

239 The temporal patterns of temperature records covering the entire Holocene (i.e., 11-1 ka) show strong
 240 differences between continents (Fig. 3). Europe shows a pronounced Mid-Holocene temperature
 241 maximum of $+1.3 \pm 0.4^\circ\text{C}$ for T_{July} at 5.7 ka while the T_{ann} maximum is less pronounced ($+0.9 \pm 0.4^\circ\text{C}$ at
 242 5.8 ka). The Mid-Holocene T_{July} was weaker and occurred earlier in Eastern North America ($+0.5 \pm 0.2^\circ\text{C}$
 243 at 7.0 ka) while T_{ann} warming was $+0.7 \pm 0.3^\circ\text{C}$ at the same time period (7.0 ka). Asia (T_{July}) and Western
 244 North America (T_{ann}) show almost no maximum but only some variations around a continuously
 245 increasing Holocene trend, with a higher increase rate before 6 ka than after 6 ka.

246 Aside from these differences among (sub-)continents, certain regional differences exist. Early Holocene
247 cold climate anomalies were most pronounced in latitudes between 45°N and 65°N, particularly in
248 Northern Europe, Northeastern Asia, and Alaska (Fig. 4) with above 2.5°C deviation to Holocene T_{ann}
249 maximum values in most records. The most pronounced T_{ann} maximum (more than 1.5°C warmer than
250 the Late Holocene) can be found in Europe north of 60°N and Eastern North America between 60°N
251 and 70°N, forming a circum-North Atlantic pattern (Fig. 5). Records from Eastern Europe, inner Asia,
252 and Southern North America show mostly no Mid-Holocene temperature maximum, but rather a Late
253 Holocene maximum. Records with an Early Holocene maximum dominate the north-central part of North
254 America and China, though these areas are characterized by high spatial variability. High ranges of
255 Holocene temperature variations (larger than 5°C) are found in mid-latitude Europe, Western Canada,
256 Southeastern US, and along the north Asian Pacific coast.

257 The averaged Northern Hemisphere north of 30°N time-series of all records that cover the entire
258 Holocene (Fig. 3) indicate that mean T_{July} was lowest at the beginning of the Holocene ($-0.7\pm 0.2^\circ\text{C}$
259 compared to present), increased until 7 ka ($+0.5\pm 0.1^\circ\text{C}$ compared to present), and slightly decreased
260 afterwards to reach modern temperatures. T_{ann} was also lowest at the beginning of the Holocene ($-$
261 $1.4\pm 0.2^\circ\text{C}$ compared to present) and reached its maximum of $0.3\pm 0.2^\circ\text{C}$ compared to present at 6.5 ka.

262 Finally, our revised global temperature curve includes all of our records and those of the Temp12k
263 dataset (Kaufman et al., 2020b) that cover the entire Holocene (in total, excluding duplicate pollen
264 records, 1098 records). It shows that mean T_{ann} was lowest during the Early Holocene at 10.5 ka with a
265 $-0.3\pm 0.3^\circ\text{C}$ anomaly relative to 1 ka and warmest at 6.6 ka with a warming of $0.3\pm 0.3^\circ\text{C}$. For the Northern
266 Hemisphere extratropics (30-80°N), we find that mean T_{ann} was lowest during the Early Holocene at
267 10.5 ka with a $-0.3\pm 0.1^\circ\text{C}$ anomaly relative to 1 ka and warmest at 6.4 ka with a warming of $0.08\pm 0.04^\circ\text{C}$.

268 The linear trends of all zonal means are significantly different ($p < 0.01$) for both T_{July} (Table A2) and T_{ann}
269 (Table A3). While the uncertainty range is small in the mid-latitudes they are larger for the 30-40°N zonal
270 band (T_{July}) and especially for the polar region (T_{July} and T_{ann} ; Fig. A3). The linear trends for T_{July} for all
271 continental means are significantly different, despite overlapping uncertainty ranges for several zonal
272 bands, e.g. 40-50°N and 50-60°N in Western North America (Fig. A4); 30-40°N and 50-60°N in Eastern
273 North America (Fig. A5), 30-40°N and 40-50°N, as well as 50-60°N and 60-70°N in Asia (Fig. A7). Large
274 uncertainty ranges can be found in the 30-40°N zonal band (Europe, Fig. A6) and the polar region
275 (Western North America, Fig. A4; Asia, Fig. A7). The linear trends for T_{ann} reveal similarities between
276 the weighted means of Europe and Asia (Europe vs. Asia: $p = 0.08$; Asia vs. Europe: $p = 0.9$; Table A5).
277 For overlapping uncertainty ranges similar patterns compared to those of T_{July} can be found, except for
278 Eastern North America, where the zonal means of 30-40°N and 50-60°N are very different to each other,
279 especially in the Early and Mid-Holocene (Fig. A5). Similar to T_{July} , the largest uncertainty ranges can
280 be found either in the 30-40°N or the 70-80°N zonal bands. For the weighted continental means the
281 uncertainty ranges of Western and Eastern North America show a strong overlap, i.e. the T_{July} mean of
282 Eastern North America mirrors the weighted Northern Hemisphere T_{July} mean. T_{July} in Asia is lower
283 overall while in Europe it is higher overall than the Northern Hemispheric mean, but the uncertainty
284 range of both continental means are larger than those in North America (West and East) and the

285 Northern Hemisphere. For T_{ann} the uncertainty ranges in all continents show a stronger overlap than for
286 T_{July} with pronounced differences between the Western and the Eastern part of North America (Fig. A8).

287

288 **3.2 Spatio-temporal pattern of precipitation reconstructions**

289 Holocene mean P_{ann} variations (as % of modern value) averaged across the Northern Hemisphere
290 extratropics have patterns that are mostly similar to T_{ann} with P_{ann} being lowest during the Early Holocene
291 ($-11.6 \pm 2.8\%$ at 11 ka compared to 1 ka) and increasing until 5.9 ka before becoming relatively stable
292 (Fig. 3).

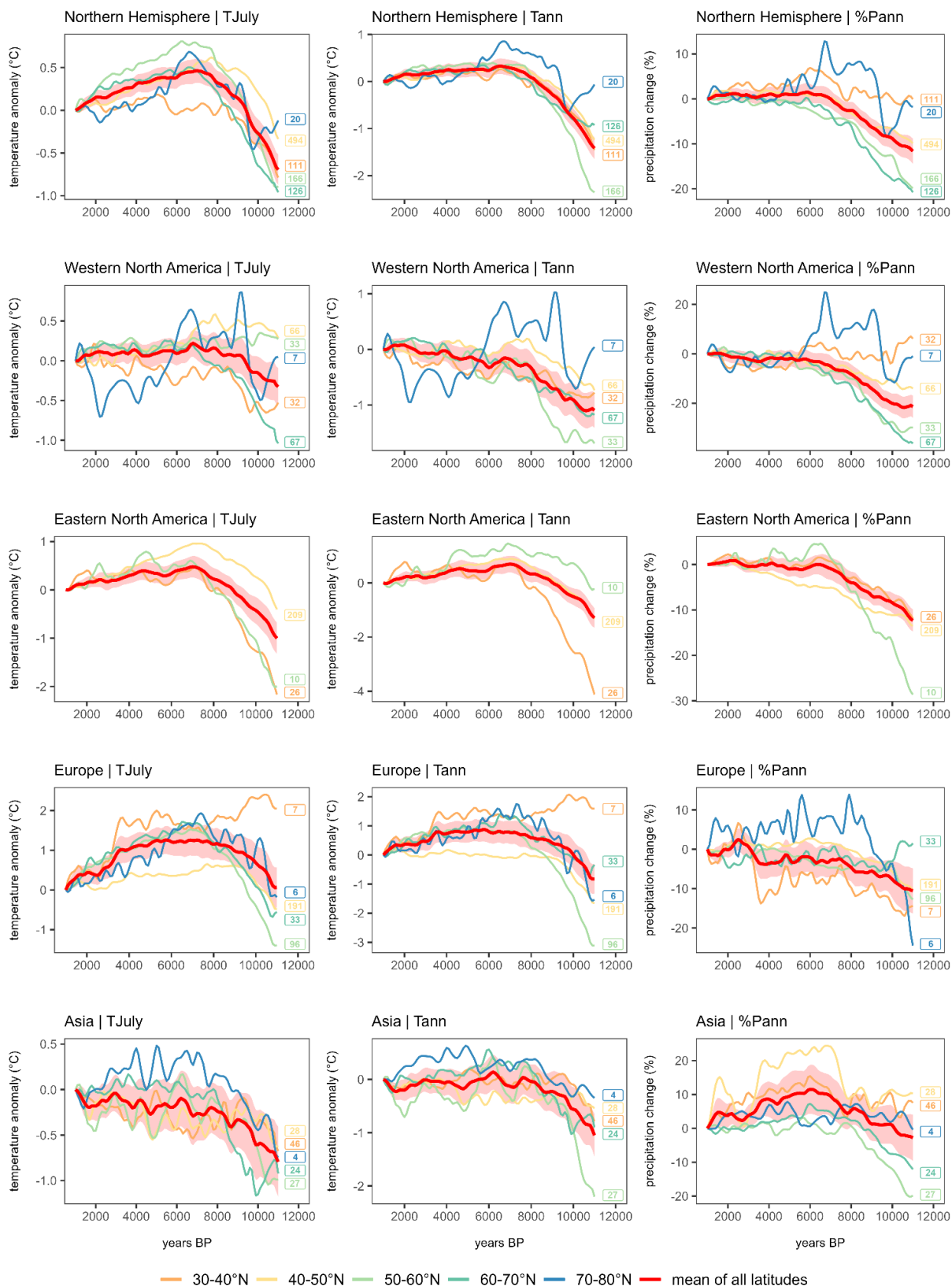
293 In contrast to the averaged Northern Hemisphere pattern, the (sub-)continental precipitation patterns
294 differ from their respective temperature patterns. The mean precipitation time-series of Western North
295 America and Europe increases from the Early Holocene to the Late Holocene; averaged Eastern North
296 America precipitation increased until 6.5 ka and varies slightly around modern values from then; and
297 Asia shows a pronounced maximum between 7 and 5 ka.

298 Time-series maps of latitudinal means and differences (Fig. 4) reveal strong spatial patterns, particularly
299 for Asia. The latitudinal mean time-series in Asia show a strong increase toward the Mid-Holocene of
300 mostly $>10\%$. After ca. 7 ka, certain differences exist: while the 70°N mean shows no clear further trend,
301 the other mean curves show a precipitation maximum which is at least 5% above the Late Holocene
302 minimum. Precipitation maxima (compared with the Late Holocene) are more pronounced and occur
303 later at lower latitudes. Furthermore, the 6-1 ka difference maps reveal that the Mid-Holocene moisture
304 maximum in subtropical Asia was most pronounced in East-central China with many records even
305 showing $\geq 50\%$ higher values at 6 ka compared to 1 ka (Fig. 4).

306 The Holocene precipitation increase in the other (sub-)continents is particularly strong in the $30\text{-}40^\circ\text{N}$
307 bands in subtropical Europe and mid-latitude North America with $>13\%$ and $>20\%$ precipitation increase,
308 respectively. In Europe and Western and Eastern North America the records from $70\text{-}80^\circ\text{N}$ show an
309 Early Holocene precipitation maximum (particularly pronounced in Alaska), which is in contrast to the
310 trends in almost all other latitudinal bands.

311 Comparing the linear trends for all zonal means reveals significant differences in all zonal bands for
312 Europe and Eastern North America ($p < 0.01$). Similarities in the trends can be found in Western North
313 America ($70\text{-}80^\circ\text{N}$ vs. $30\text{-}40^\circ\text{N}$: $p = 0.06$) and especially in Asia, where several combinations of zonal
314 trends are not significantly different (i.e. $30\text{-}40^\circ\text{N}$ vs. $40\text{-}50^\circ\text{N}$ ($p = 0.08$) and $30\text{-}40^\circ\text{N}$ vs. $70\text{-}80^\circ\text{N}$ ($p =$
315 0.76)). For details, see Table A4. All trends in the continental precipitation means are found to be
316 different ($p < 0.01$; Table A5). The uncertainty ranges for all latitudinal means are small, except for the
317 $70\text{-}80^\circ\text{N}$ zonal band in the polar region ($\%P_{\text{ann}}$; Fig. A3). In Western North America the zonal means of
318 $50\text{-}60^\circ\text{N}$ and $60\text{-}70^\circ\text{N}$ show a strong overlap in their uncertainty ranges and the largest uncertainty range
319 can be found in the polar region (Fig. A4). In Europe and Asia, the mid-latitudes show the smallest
320 uncertainty ranges, while the southernmost and northernmost zonal bands have higher uncertainty
321 ranges (Fig. A6 and A7). Notable is the $40\text{-}50^\circ\text{N}$ zonal band in Asia, which shows the highest uncertainty
322 range of all continental zonal bands, especially in the Mid-Holocene (Fig. A7). Compared to the Northern

323 Hemispheric mean, the continental %P_{ann} mean of Eastern North America shows the smallest deviations,
 324 although the continental mean only comprises the zonal bands between 30°N and 60°N. Precipitation
 325 changes in Western North America are overall lower than the Northern Hemispheric mean, while the
 326 precipitation changes in Asia are overall higher (Fig. A8).

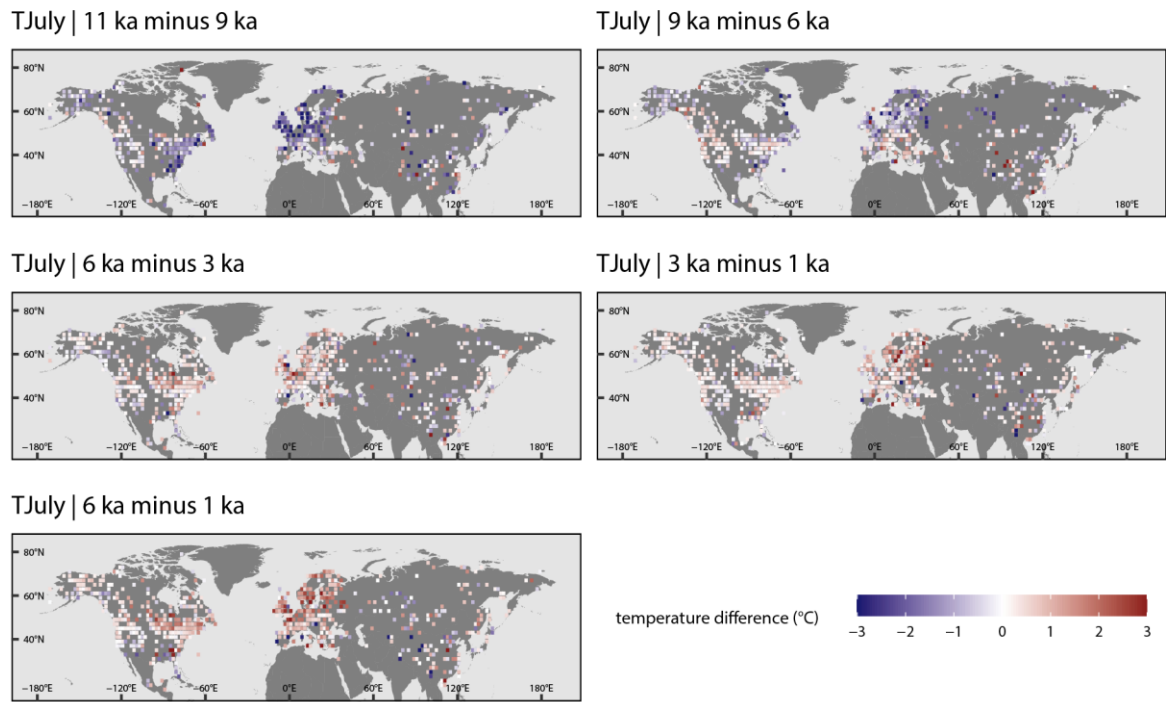


— 30-40°N — 40-50°N — 50-60°N — 60-70°N — 70-80°N — mean of all latitudes

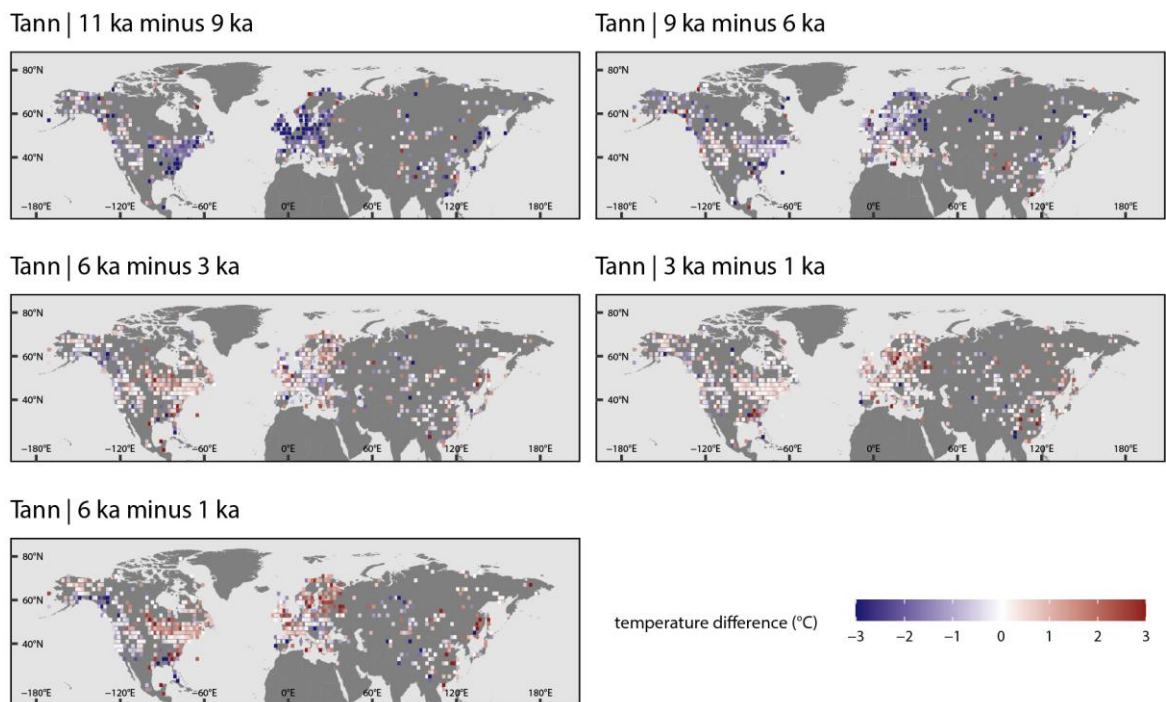
327

328 **Figure 3. Hemispheric, (sub-)continental, and zonal mean curves for T_{July} , T_{ann} , and $\%P_{ann}$ derived**
 329 **from pollen-based reconstruction with WA-PLS. Curves from zonal bands that contain fewer than**
 330 **three grid cells were excluded. The shading corresponds to the latitude-weighted standard error of the**
 331 **latitude-weighted mean. Labels in corresponding colors indicate the number of grid boxes that**
 332 **contributed to each latitudinal curve.**

333

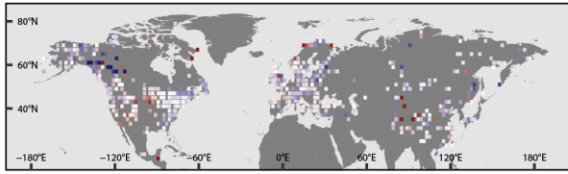


334

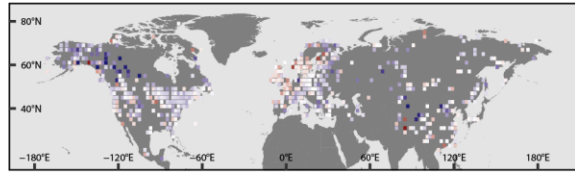


335

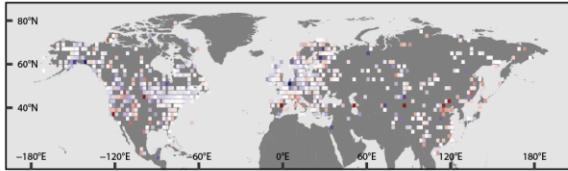
%Pann | 11 ka minus 9 ka



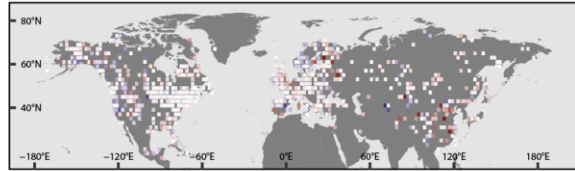
%Pann | 9 ka minus 6 ka



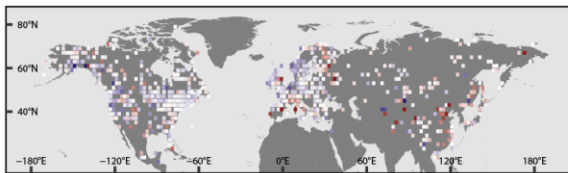
%Pann | 6 ka minus 3 ka



%Pann | 3 ka minus 1 ka



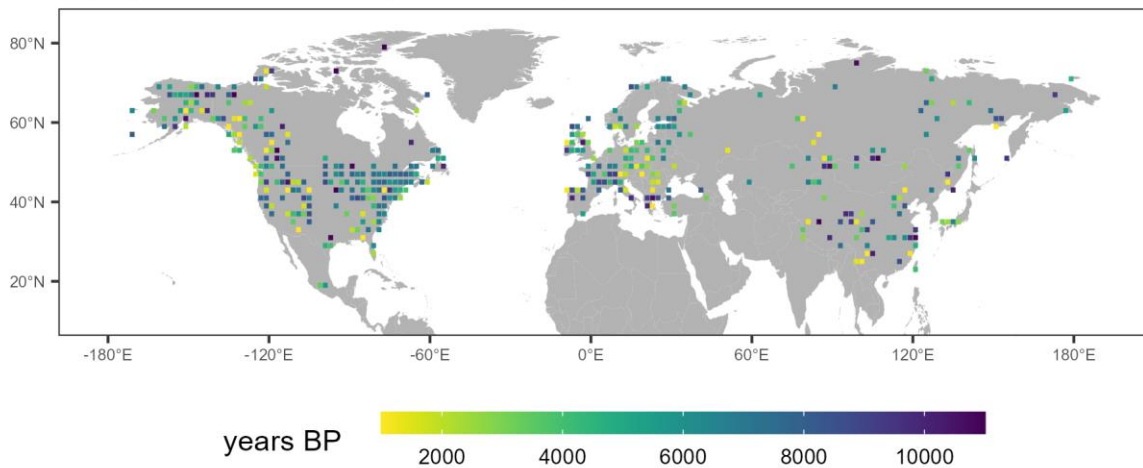
%Pann | 6 ka minus 1 ka



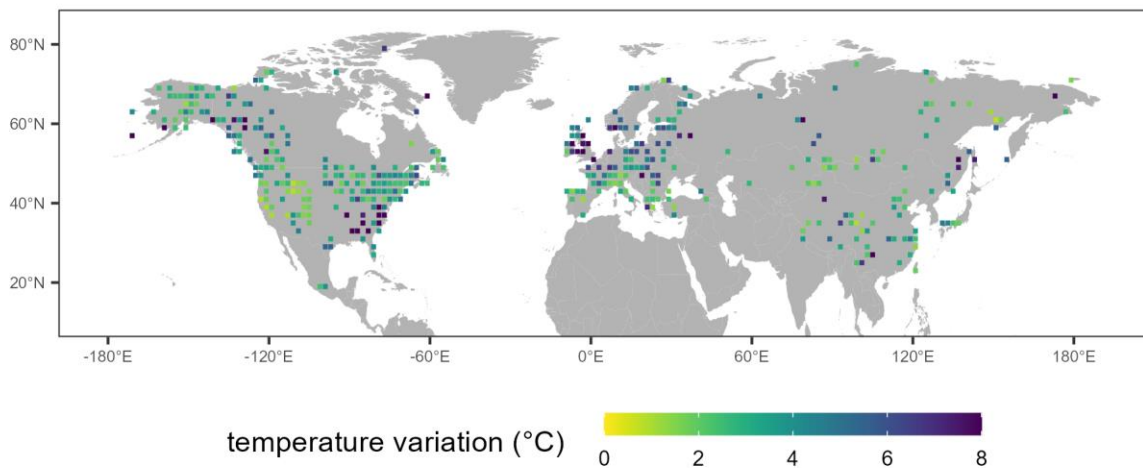
336

337 **Figure 4. Difference maps of T_{July} , T_{ann} ($^{\circ}C$), and P_{ann} (as % of the value of the younger time-slice)**
338 **between selected time-slices.** Color code for values outside the range were restricted to range maxima.
339 A list with the entire value range and the proportions of values that fall within the restricted range are
340 presented in Table A1. Maps are gridded values averaging the values of records from within the $2^{\circ} \times 2^{\circ}$
341 grid cell.

LegacyClimate 1.0 Dataset | Holocene temperature maximum

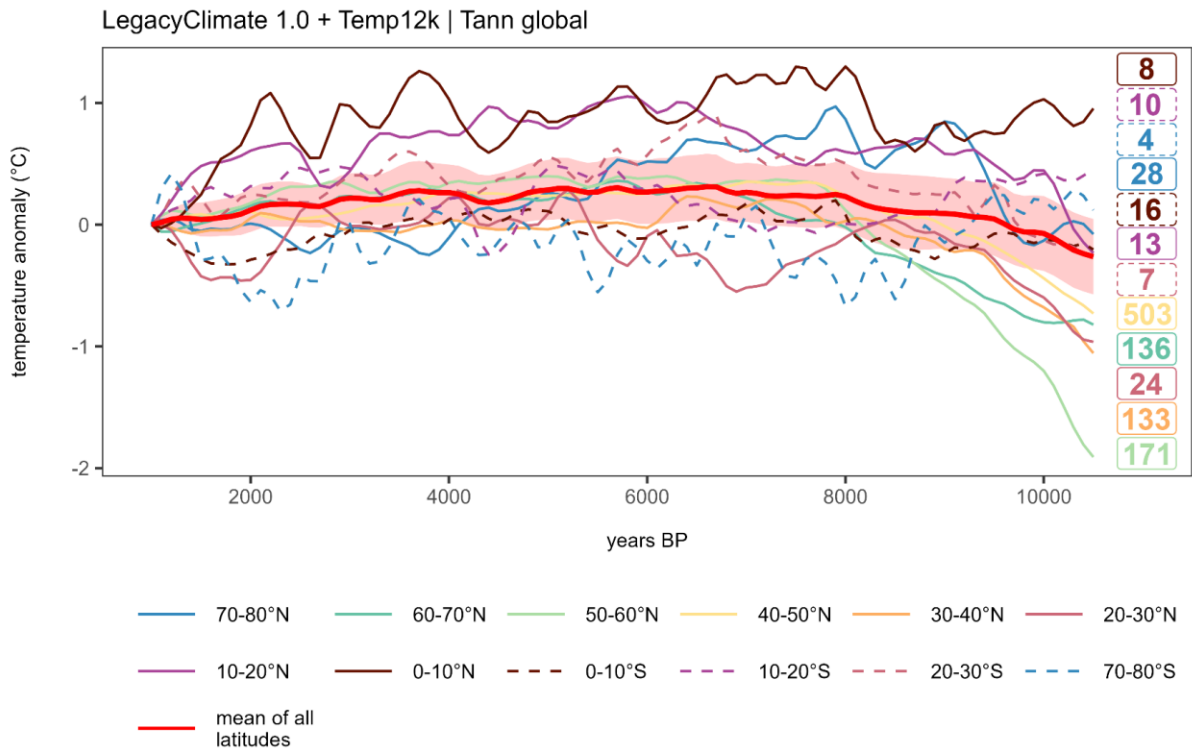
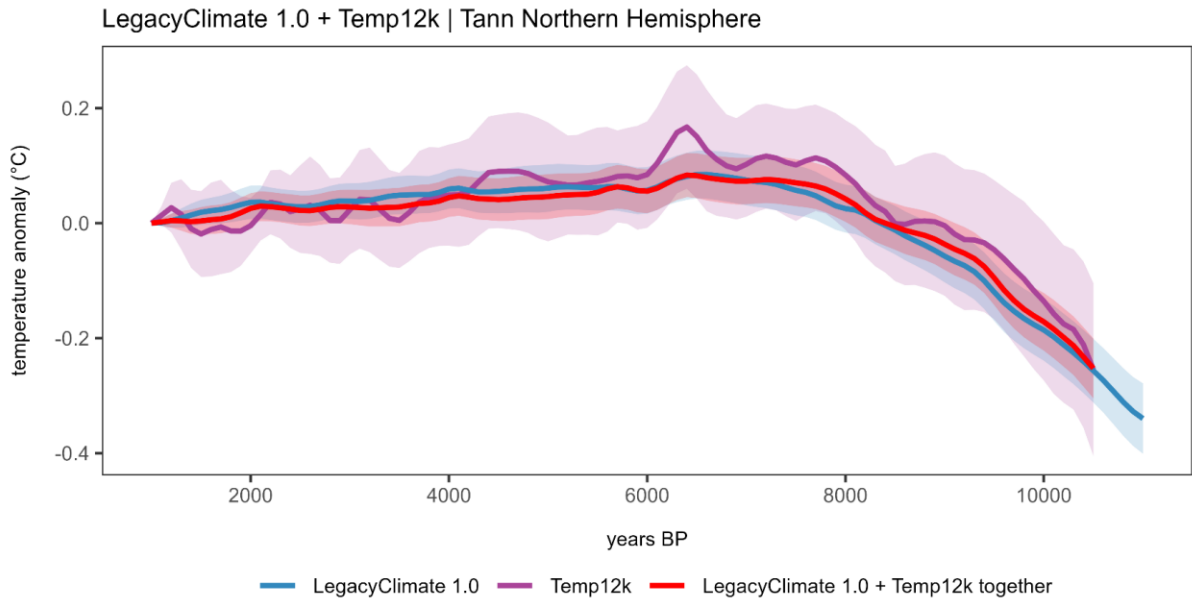


LegacyClimate 1.0 Dataset | Temperature variation during the Holocene



342

343 **Figure 5. Maps indicating the timing of the T_{ann} maximum (top) and the range of T_{ann} variation**
344 **during the Holocene (11-1 ka, bottom).** Each $2^\circ \times 2^\circ$ grid cell contains the averaged values of all
345 records located within one grid cell. For each grid cell, the T_{ann} variation was determined as the range
346 between minimum and maximum T_{ann} anomalies. The T_{ann} Holocene temperature maximum is the timing
347 of the anomaly maximum. Color code for values outside the range were restricted to range maxima.



348

349 **Figure 6. Mean curves for temperature.** (top) Northern Hemisphere weighted means with shaded
 350 weighted standard error (no curves for latitudes): LegacyClimate 1.0 (n=957; blue), Temp12k dataset
 351 (n=272, see methods for record filter; purple), LegacyClimate 1.0 + Temp12k mean (n=1098; red);
 352 (bottom) LegacyClimate 1.0 + Temp12k global mean with latitudinal means. Labels in corresponding
 353 colors indicate the number of grid boxes that contributed to each latitudinal curve.

354

355

356

357 **4 Discussion**

358 **4.1 Spatial temperature pattern (in light of the global Holocene temperature curve)**

359 The general pattern of the LegacyClimate 1.0 mean annual temperature curve of the Northern
360 Hemisphere extratropics agrees with those of previous investigations (Marcott et al., 2013; Kaufman et
361 al., 2020b; Kaufman and Broadman, 2023) including a cold Early Holocene, a temperature maximum
362 during the Early to Mid-Holocene, and a slight cooling towards the present-day (Fig. 2; Fig. A8). Orbital
363 forcings are assumed to have an important influence on the trends in the global mean temperatures,
364 which led to feedback mechanisms like decreased polar sea ice or shifted vegetation ranges and thus
365 to increased temperatures during the Mid-Holocene (Kaufman and Broadman, 2023). Subsequently,
366 changes in solar irradiance, an increasing albedo due to land-cover changes and increasing volcanic
367 activity probably contributed to a global cooling during the Late Holocene (Kaufman and Broadman,
368 2023). Both our LegacyClimate 1.0 and the Temp12k mean temperature curves increase from the Early
369 Holocene to the Mid-Holocene by about 0.4°C when the same stacking approach is applied. However,
370 the LegacyClimate 1.0 stack shows only a minimal temperature decline between the early Mid-Holocene
371 maximum and the Late Holocene minimum of ~0.08°C compared to ~0.17°C in the Temp12k stack. We
372 suggest two probable reasons for this finding: 1) a more complete spatial and temporal
373 representativeness of the dataset, and 2) a unique methodology to reconstruct a small set of climate
374 variables from pollen data.

375 First, our mean annual temperature curve includes about four times as many records as the Temp12k
376 dataset (957 records in the LegacyClimate 1.0 dataset vs. 272 records in the Temp12k dataset,
377 Kaufman et al. 2020b; Fig. 1). In particular, Asia is represented by substantially more records in the
378 combined dataset. Our temperature reconstruction from Asia shows an average trend that differs from
379 the overall Northern Hemisphere trend as it has no pronounced Holocene temperature maximum (Fig.
380 A8; Table A6). This is particularly true for Asian T_{ann} records south of 50°N and T_{July} records south of
381 60°N. This feature has not been recognized so far, likely because Asian temperature reconstructions
382 are mostly lacking in previous compilations (e.g., Marcott et al., 2013; Marsicek et al., 2018; Routson et
383 al., 2019; Kaufman et al., 2020b). Even if the Mid- to Late Holocene cooling trend observed in Asia north
384 of 60°N (Fig. 2) agrees with the proposed Neoglacial (sub-)arctic-wide Holocene cooling, the amount of
385 cooling of <0.5°C is low compared to the cooling observed in other regions (e.g., in Europe where an
386 average cooling of ~1.5°C has been reconstructed; McKay et al., 2018; Fig. 2). As with the differences
387 between Eastern and Western Eurasia, we find a difference between Eastern and Western North
388 America. In particular, we can identify a circum-North Atlantic pattern with a strong Early Holocene
389 increase, a pronounced Mid-Holocene maximum and strong temperature range, and a circum-North
390 Pacific pattern with an overall weak change. This is likely related to the impact of the decaying Laurentide
391 ice-sheet on the North Atlantic which was probably a stronger driver of Early to Mid-Holocene temperature
392 change than insolation (Renssen et al., 2009; Renssen et al., 2012; Zhang et al., 2016).

393 Even if this study shows a less pronounced Holocene temperature maximum, the problem remains that
394 this does not align with the overall Holocene increase in the mean global (and Northern Hemisphere)
395 temperature revealed by Earth System Models. Our study points to a strong regionalization of Holocene

396 temperature trends and range of variation in the Northern Hemisphere extratropics, which was also
397 reported in recent studies (e.g. Kaufman et al., 2020b; Osman et al., 2021; Cartapanis et al., 2022). This
398 somehow contradicts the ‘Holocene conundrum’ concept which tackled Holocene temperature change
399 mainly by analyzing the global mean and understanding the differences between proxy-based and
400 simulated reconstructions. However, the conundrum debate has since progressed and recent studies
401 hint at discrepancies in data-model comparisons due to spatiotemporal dynamics related to
402 heterogeneous responses to climate forcing and feedbacks (e.g., the timing of a Holocene thermal
403 maximum between reconstructions from continental and from marine proxy records; Cartapanis et al.,
404 2022). Our finding is in line with recent modeling approaches, which also yield strong regional
405 differences in temperature developments (Bader et al., 2020) allowing for a regional comparison. Recent
406 paleo-data assimilation approaches based on marine temperature reconstructions reveal peculiarities
407 of spatial averaging as one reason for the model-data mismatch (Osman et al., 2021). The error is most
408 pronounced where the number of included records is small. This stresses the importance of good spatial
409 coverage of the records used for the assessment of the mean temperature trend. Including terrestrial
410 reconstructions is crucial. Compared with previous syntheses of terrestrial records, our compilation is
411 notable for its higher record density in Asia, a region for which Earth System Models show diverging
412 past climate changes, highly sensitive to boundary conditions and forcing (Bakker et al. 2020; Brierley
413 et al., 2020; Lohmann et al. 2021). Therefore, our reconstruction makes a decisive contribution to
414 locating and clarifying the model-data mismatch in the Northern Hemisphere extratropics. From a proxy
415 perspective, future targets of synthesis studies should focus on the Southern Hemisphere and poorly
416 covered areas in Central Asia and Siberia.

417 Second, standardized methodologies may have contributed to the observed differences between the
418 LegacyClimate 1.0 mean T_{ann} curve and the Temp12k curve. Our T_{ann} reconstruction only includes
419 records of mean annual temperature while the Temp12k product mixes reconstructions of seasonal
420 temperature (mostly T_{July}) if T_{ann} is not available from a site. This assumption of equivalence between
421 annual and summer temperature at any given site can impact the trend and amplitude of the stacks. A
422 seasonal bias in the reconstructions may originate from a real, larger Holocene range of summer
423 temperature variations (Bova et al., 2021) or is an artefact introduced by having a larger T_{July} range
424 covered by the calibration datasets compared with T_{ann} which is, however, not the case in our calibration
425 sets.

426 Our pollen-based reconstructions are all performed with WA-PLS, which is known to produce smaller
427 climate amplitudes than MAT (a likewise commonly used method) because it is less sensitive to extreme
428 climate values in the modern pollen dataset (Birks and Simpson 2013; Cao et al., 2017; Nolan et al.
429 2019). Furthermore, by using a standard area size for our modern pollen datasets, we may have
430 stabilized the regional reconstructions, that is, equalized the amplitude as the source areas represent
431 rather similar biogeographical and climate ranges. Finally, our reconstructions include only records that
432 cover the entire Holocene period (11-1 ka) and not just parts of it. Hence, all time-slices have a similar
433 spatial coverage and the temporal pattern is not biased by regions where archives are only available in
434 certain periods (e.g., the Late Holocene peatland establishment).

435 As with all applications of taxa-based transfer functions to fossil records, we assume that both modern
436 and past taxa assemblages (in our case, vegetation) are in equilibrium with climate, and that the
437 relationships inferred from modern data do not change throughout the Holocene (Birks et al., 2010;
438 Chevalier et al., 2020) and that the modern pollen assemblages are not heavily biased by human impact.
439 Differences in global boundary conditions during the Early to Mid-Holocene (e.g., lower atmospheric CO₂
440 concentration, different seasonal insolation) however, may have modified these relationships, which
441 could have also dampened the reconstructed amplitudes. Also, vegetation response to climate change
442 may be involve lags (see the ongoing discussion about the so-called 'forest conundrum', i.e., the
443 observation that observed forest maximum lags the simulated temperature maximum; Dallmeyer et al.,
444 2022) and depends on the initial conditions such as the distribution of refugia during the Last Glacial
445 (Herzschuh et al., 2016; 2020). Furthermore, there are areas, especially the densely settled regions in
446 Europe and Southeastern Asia, that are affected by human activities throughout the Holocene due to
447 intense animal husbandry, as inferred from the abundance of Plantaginaceae and Rumex as indicators
448 of grazing (Herzschuh et al., 2022a), or due to industrialization since the second half of the 19th century.
449 This probably led to extinction events, especially for disturbance-dependent taxa and contributed to
450 gaps within the potential bioclimatic space of taxa that form natural communities (Zanon et al., 2018).
451 The absolute effect of these biases is hard to quantify (but see Cleator et al., 2020), and many
452 comparative, multi-proxy Holocene studies have shown that pollen-based reconstructions are as reliable
453 as any other proxy (Kaufmann et al., 2020a; Dugerdil et al., 2021). In contrast, one advantage of single
454 proxy studies is that any biases will affect all the records similarly. As such, even if the actual amplitude
455 of our regional and global stacks might be dampened, the trends and spatial patterns shared by the data
456 are likely to remain correct.

457

458 **4.2 Spatio-temporal precipitation pattern**

459 Our analyses of the Holocene spatio-temporal precipitation pattern fill a research gap, as syntheses of
460 proxy-based precipitation change on a hemispheric scale during the Holocene are still lacking. Regional
461 syntheses are available for Europe (Mauri et al., 2014 and 2015), North America (Ladd et al., 2015;
462 Routson et al., 2021), and Eastern Asia (Herzschuh et al., 2019). Interestingly, we observed a similar
463 pattern for Northern Hemisphere-wide averaged Holocene trends of P_{ann} and T_{ann} , but differences
464 among corresponding P_{ann} and T_{ann} curves at (sub-)continental and latitudinal scales, e.g., in Asia, where
465 the P_{ann} means are overall higher than the Northern Hemispheric means while the T_{ann} means are overall
466 lower since ~ 9 ka (Fig. A8), or for the 30-40°N zonal band, where T_{ann} shows an Early to Mid-Holocene
467 warming while no trend in the P_{ann} means could be found for this time period (Fig. A3).

468 This regional heterogeneity with respect to the precipitation trend (i.e., significantly different trends for
469 the Northern Hemisphere except for some regions in Asia, Table A4, Fig. A8) is also seen in recent
470 Earth System Model simulations for the last 8000 years (Mauri et al., 2014; Dallmeyer et al., 2021).
471 Although the simulated pattern does not exactly match our reconstructions, they share many similar
472 structures such as high precipitation in the Early and Mid-Holocene in East Asia (Fig. 4). For this region,
473 our reconstruction shows the strongest Mid- to Late Holocene precipitation decline worldwide, reflecting

474 the weakening of the East Asian Summer Monsoon (EASM) in response to the decrease in summer
475 insolation. This trend in moisture has been confirmed by earlier qualitative and quantitative proxy
476 syntheses and modeling studies (Wang et al., 2010; Zheng et al., 2013; Liu et al., 2014a; Herzschuh et
477 al., 2019).

478 In contrast, many Central Asian sites show low Early-Holocene precipitation levels (Fig. 4). This anti-
479 phase relationship in EASM to Central Asian moisture change is in line with earlier studies (Jin et al.,
480 2012; Chen et al., 2019; Herzschuh et al., 2019; Zhang et al., 2021). The causal mechanisms are still
481 debated. Among other reasons, precipitation-evaporation effects (Herzschuh et al., 2004; Zhang et al.,
482 2011; Kubota et al., 2015), transcending air mass related to the Rodwell-Hoskins response to
483 monsoonal heating (Herzschuh et al., 2004; Wang et al., 2017), effects from winter precipitation (Li et
484 al., 2020), and translocation of the westerly jetstream (Herzschuh et al., 2019) may contribute to the
485 anti-phased precipitation change.

486 Arctic warming mechanistically should be linked with wetting in the Arctic due to high hydrological
487 sensitivities (Trenberth, 2011). Such a pattern is, for example, obvious for Early to Mid-Holocene climate
488 change in most records from Alaska. Interestingly, several records from the northern Arctic coastal
489 region in Russia, northern Norway and Canada show a wet Early Holocene, which is also observed in
490 simulations (Dallmeyer et al., 2021).

491 Contrasting the trend in the East Asian monsoon region (Fig. 2; Fig. A7), annual precipitation increases
492 in mid-latitude Europe during the Holocene according to our reconstructions (Fig. 2; Fig. A6). Routson
493 et al. (2019) propose a circum-hemispheric mid-latitude rise of moisture levels over the Holocene
494 based on a semi-quantitative dataset that is strongly concentrated around the circum-Atlantic region.
495 They relate the decreased net precipitation to the weakened Early Holocene latitudinal temperature
496 gradient. Due to polar amplification, the arctic regions experienced a stronger warming in the climate
497 compared to the equatorial region, which is also supported by our dataset. However, we also see in our
498 reconstructions that this view is too general, but it may explain the precipitation response in Europe as
499 the weakening of the latitudinal temperature gradient is particularly pronounced in Europe in our
500 reconstructions. This change in temperature pattern is probably a result of a dampening in the cyclonic
501 activity along the weaker westerly jet (Chang et al., 2002; Routson et al., 2019; Xu et al., 2020), bearing
502 less precipitation during the Early Holocene compared to modern conditions. With the strengthening of
503 the latitudinal temperature gradient towards the Late Holocene, cyclonic activity enhances, leading to
504 an increase of precipitation over the Holocene.

505 According to our reconstructions, the precipitation trend in Eastern and Western North America strongly
506 differs ($p < 0.01$; Table A5; Fig. A3). While in the Eastern part the mean precipitation level is relatively
507 stable in all latitudinal bands, except the 50-60°N zonal band, over the Holocene (Fig. A5), precipitation
508 strongly increases on average in the Western part (Fig. A4), driven by a precipitation rise in the mid-
509 latitudes (40-70°N). In the polar regions and south of 40°N, precipitation declines from the Mid-Holocene
510 (Fig. 4; Fig. A4). The latter may be related to a decrease in the North American monsoon intensity, in
511 line with the orbital monsoon hypothesis (Kutzbach, 1981; Harrison et al., 2003). In the polar region,
512 modeling studies report northward shifted storm tracks coinciding with a northward replaced upper

513 tropospheric jetstream in the Mid-Holocene compared to the Late Holocene, promoting precipitation in
514 the arctic region and decreasing precipitation at mid-latitudes (Zhou et al., 2020; Dallmeyer et al., 2021).
515 With the southward shift of the polar jet during the Holocene, precipitation decreased in the high northern
516 latitudes in North America and increased further south (Liu et al., 2014b).

517 The rise in moisture levels across the North American continental interior over the course of the
518 Holocene has been proposed before (Grimm et al., 2001; Zhou et al., 2020; Dallmeyer et al., 2021) but
519 has not yet been quantified with continental-wide proxy-data. The main drivers of this trend are still being
520 debated: besides shifts in the westerly wind circulation (Seager et al., 2014), weakening subsidence
521 caused by teleconnection with the weakening Northern Hemispheric monsoon systems (Harrison et al.,
522 2003; Dallmeyer et al., 2021), reorganization of the atmospheric circulation around the Bermuda high
523 (Grimm et al., 2001), and changes in the sea-surface temperature pattern (Shin et al., 2006) may
524 contribute to an increase in precipitation over the Holocene.

525 Reconstructing temperature and precipitation from a single dataset implies that they are both important
526 in defining the presence and/or abundance of specific pollen taxa (Salonen et al., 2019). This hypothesis
527 cannot be tested but to some extent has been assessed by several analyses (Juggins, 2013). The WA-
528 PLS reconstruction was also applied with tailored modern calibration sets (i.e., selecting samples so
529 that the correlation between temperature and precipitation in the calibration dataset is reduced). The
530 finding that the reconstructions were generally very similar between those using the full and those using
531 the tailored modern datasets can be taken as an indication that co-variation is not a major issue in these
532 reconstructions (Herzschuh et al., 2022a). This conclusion is also supported by the fact that T_{ann} and
533 P_{ann} records that pass the reconstruction significance test when the impact of the other variable is
534 partialled out (Telford and Birks, 2011), are almost evenly distributed over the Northern Hemisphere
535 records (Herzschuh et al., 2022a). This is also confirmed by the visual inspection of the regional
536 reconstructions in Fig. 3, where we cannot detect correlations between variables within latitudinal zones,
537 as would be expected from dependent reconstructions. This suggests that our reconstructions do reflect
538 distinctive trends from the pollen data.

539

540 **5 Conclusions**

541 We investigated Holocene time-series of T_{July} , T_{ann} , and P_{ann} for the Northern Hemisphere extratropics
542 making use of 2593 pollen-based reconstructions (LegacyClimate 1.0). Compared with previous
543 datasets, we include many more records, particularly from Asia. We present mean curves obtained with
544 the same method for the Northern Hemisphere, the (sub-)continents (Asia, Europe, Eastern North
545 America, Western North America), and regional zones (i.e., 10° latitudinal bands for (sub-)continents)
546 as well as Northern Hemisphere gridded data for selected time-slices.

547 Our results indicate that Holocene climate change shows unique regional patterns. The concept of a
548 Mid-Holocene temperature maximum only applies mainly to the mid and high northern latitudes in the
549 circum-North Atlantic region while records from mid-latitude Asia, Western North America, and all
550 subtropical areas do not fit into this concept but mostly show an overall Holocene increase or other

551 patterns. As such, the ‘Holocene conundrum’, originally proposed as a global feature, may instead apply
552 to a restricted region.

553 The precipitation trend is roughly similar to the temperature trend at the hemispheric scale, in particular
554 with respect to the strong increase from the Early to Mid-Holocene. At the regional scale, the
555 precipitation trends differ from each other and also from the regional temperature trends. The 40-50°
556 latitudinal band in Asia shows the most pronounced Mid-Holocene precipitation maxima while many
557 regions show increasing Holocene trends including most of Europe and Western North America. We
558 relate these differences to regionally specific circulation mechanisms and their specific relationships
559 with temperature changes.

560 Given a background of strong regional heterogeneity, the calculation of global or hemispheric means
561 might generally lead to misleading concepts but the focus should be on understanding the spatio-
562 temporal patterns requiring spatially dense proxy-datasets for comparison with simulations.

563

564 **6 Data Availability**

565 The compilation of reconstructed T_{July} , T_{ann} , and P_{ann} , is open access and available at PANGAEA
566 (<https://doi.org/10.1594/PANGAEA.930512>; in the “Other version” section). The dataset files are stored
567 in machine-readable data format (.CSV), which are already separated into Western North America,
568 Eastern North America, Europe, and Asia for easy access and use.

569

570 **Author contributions.** UH designed the study. The analyses were led by UH and implemented by TB.
571 UH guided the interpretation of the results and collected detailed comments from AD, MC, OP, CL, and
572 RH. All co-authors commented on the initial version of the manuscript.

573

574 **Competing interests.** The authors declare that they have no conflict of interest.

575

576 **Acknowledgements.** We would like to express our gratitude to all the palynologists and geologists who,
577 either directly or indirectly by providing their work to the Neotoma Paleocology Database, contributed
578 pollen data and chronologies to the dataset. The work of data contributors, data stewards, and the
579 Neotoma community is gratefully acknowledged. We also thank Cathy Jenks for language editing.

580

581 **Financial support.** This research has been supported by the European Research Council (ERC Glacial
582 Legacy 772852 to UH) and the PalMod Initiative (01LP1510C to UH). TB, MC, and AD are supported
583 by the German Federal Ministry of Education and Research (BMBF) as a Research for Sustainability
584 initiative (FONA; <https://www.fona.de/en>) through the PalMod Phase II project (grant no. FKZ:

585 01LP1926D and 01LP1920A). CL holds a scholarship from the Chinese Scholarship Council (grant no.
 586 201908130165). NR work was supported by the Russian Science Foundation (Grant No. 20-17-00110).

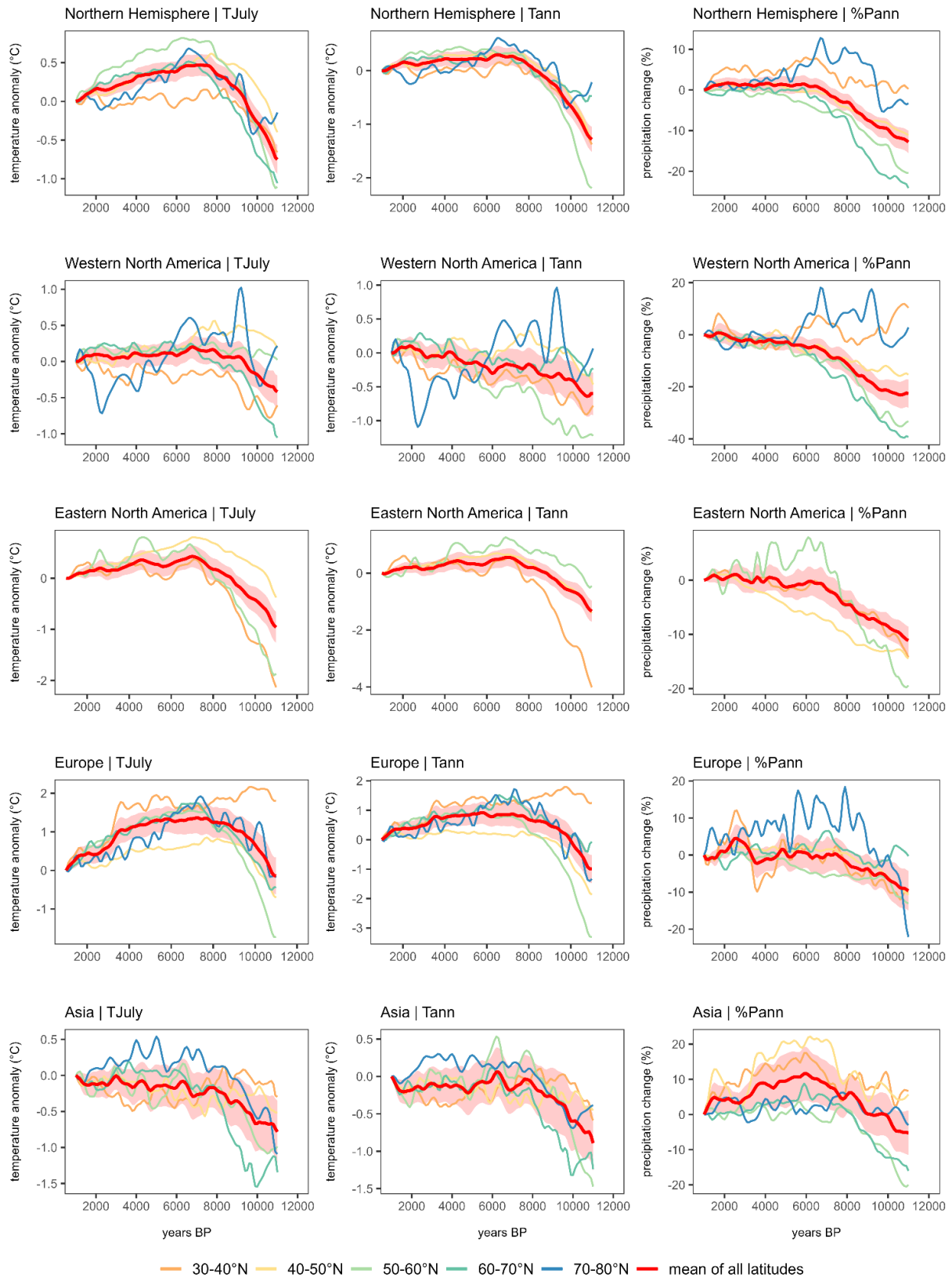
587

588 **Appendix**

589

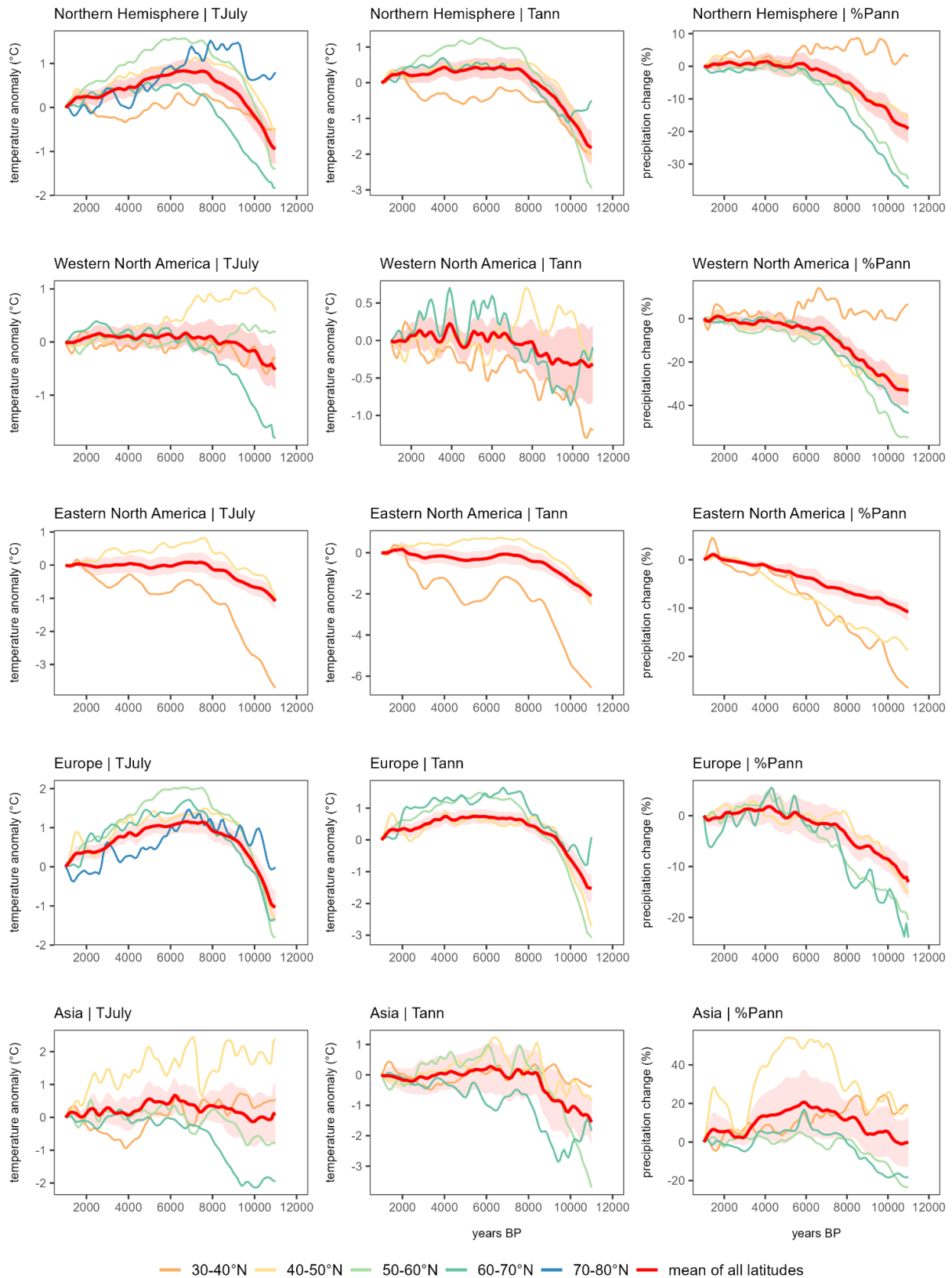
590 **Table A1.** Range of values in the difference maps (Fig. 4) and proportion of values that fall within a
 591 restricted range of -3 to +3 °C for temperature and -50% to 50% for precipitation change.

	T_{July}		T_{ann}		P_{ann}	
	Value range	% within restricted range	Value range	% within restricted range	Value range	% within restricted range
11-9 ka	-12.3°C to +8.2°C	87.8 %	-20.0°C to +6.0°C	79.7 %	-131.7% to +151.3%	96.9 %
9-6 ka	-6.1°C to +16.4°C	95.8 %	-8.9°C to +12.0°C	92.9 %	-81.4% to +103.9%	98.4 %
6-3 ka	-8.2°C to +6.4°C	98.1 %	-8.0°C to +7.9°C	96.5 %	-175.1% to +423.6%	98.8 %
3-1 ka	-10.1°C to +4.6°C	98.2 %	-11.0°C to +10.1°C	97.2 %	-1157.4% to +90.7%	99.0 %
6-1 ka	-9.6°C to +6.5°C	94.9 %	-8.9°C to +9.0°C	93.6 %	-67.6% to +694.3%	98.2 %



592

593 **Figure A1: Hemispheric, continental, and latitudinal mean curves for T_{July} , T_{ann} , and P_{ann} derived**
 594 **from pollen-based reconstruction with WA-PLS_tailored.** Latitudinal bands that contain fewer than
 595 three grid cells are not shown. The shading corresponds to the latitude-weighted standard error of the
 596 latitude-weighted mean.

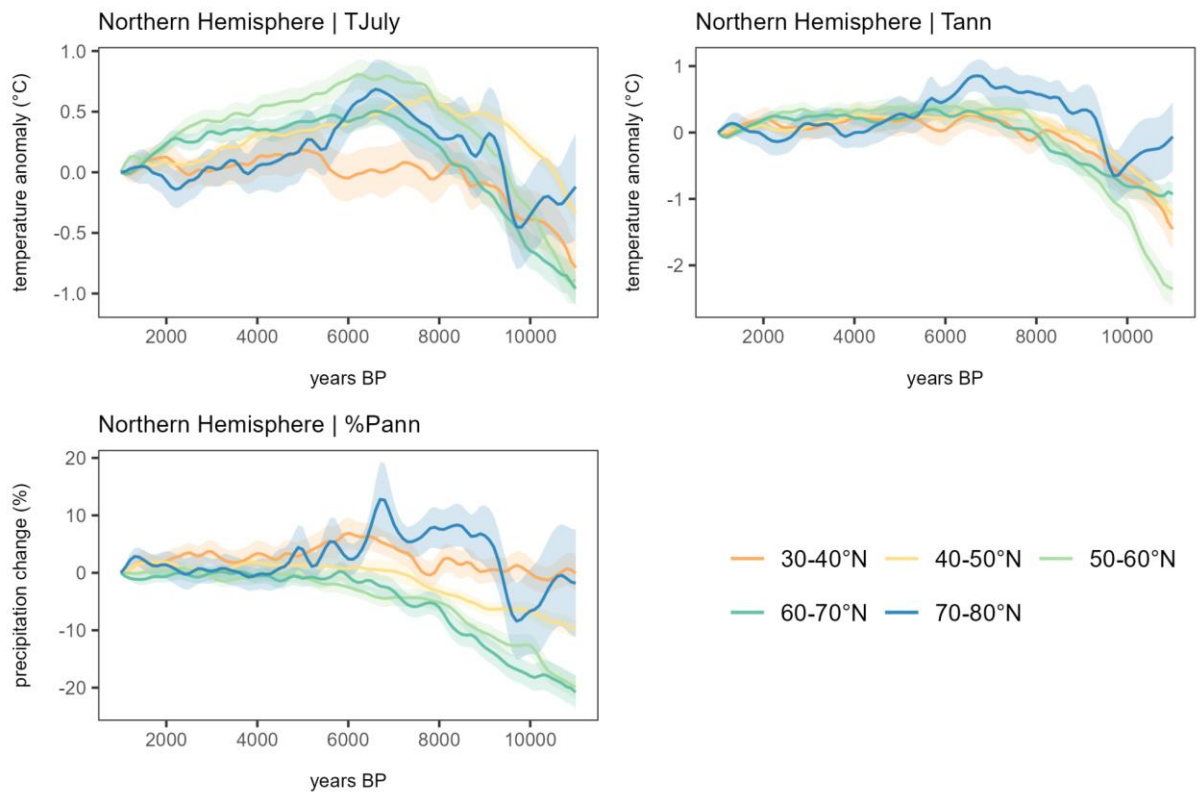


597

598 **Figure A2: Hemispheric, continental, and latitudinal mean curves for T_{July} , T_{ann} , and P_{ann} derived**
 599 **from pollen-based reconstruction with WA-PLS_tailored with significant records ($p < 0.2$).**

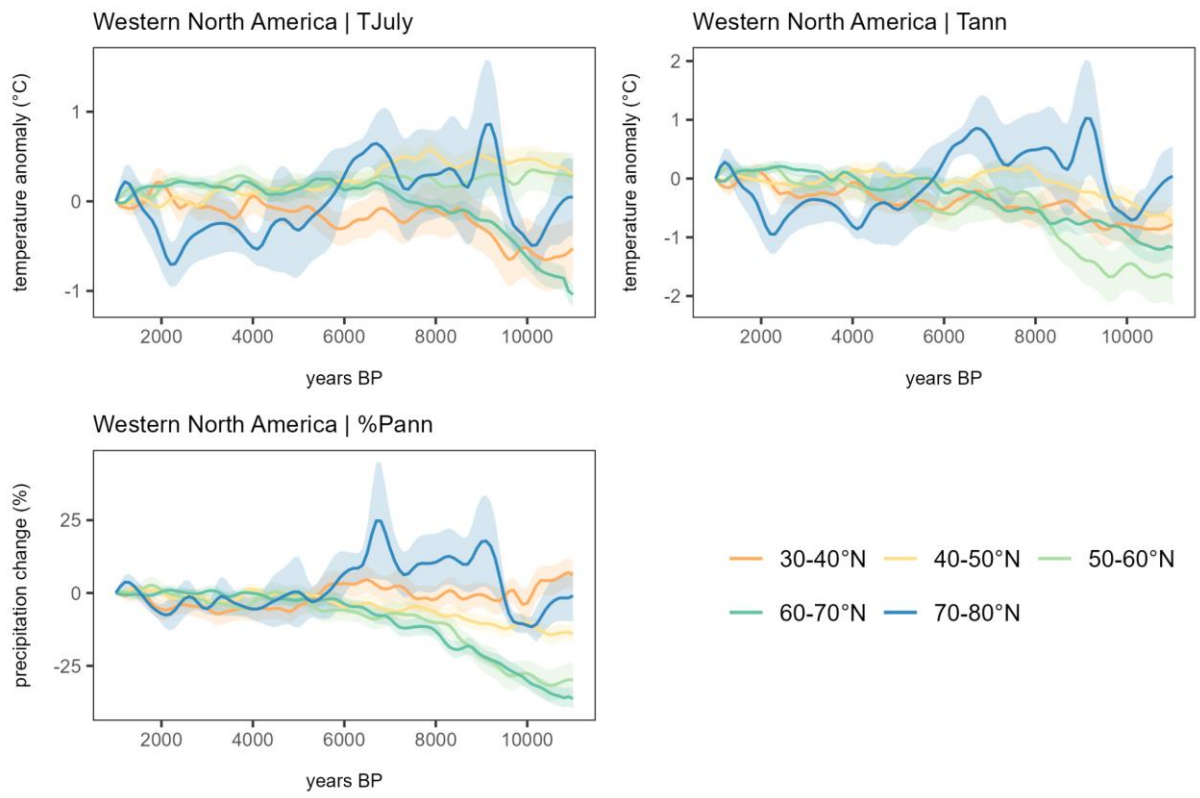
600 Latitudinal bands that contain fewer than three grid cells are not shown. The shading corresponds to the

601 latitude-weighted standard error of the latitude-weighted mean.



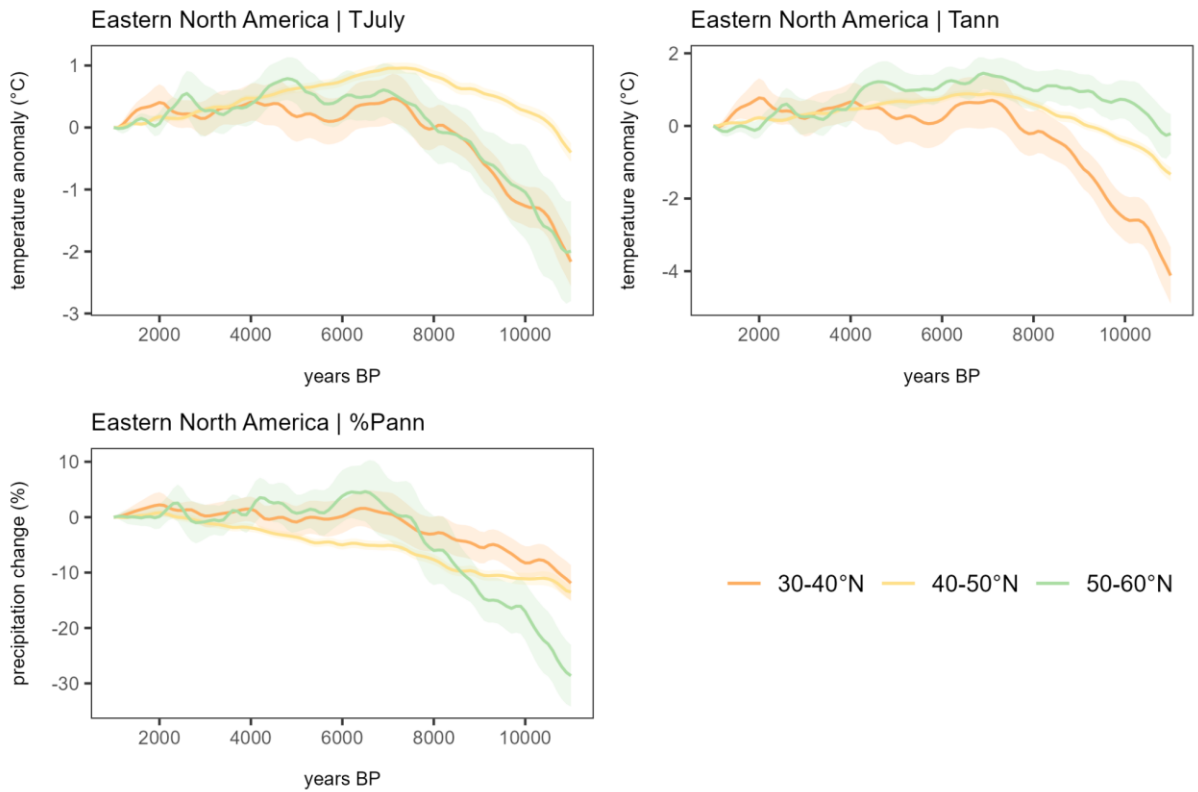
602
 603
 604
 605
 606

Figure A3: Northern Hemispheric latitudinal mean curves with shaded standard errors for T_{July} , T_{ann} , and $\%P_{ann}$ derived from pollen-based reconstruction with WA-PLS (latitudinal bands that contain fewer than three grid cells are not shown).



607
 608
 609
 610
 611

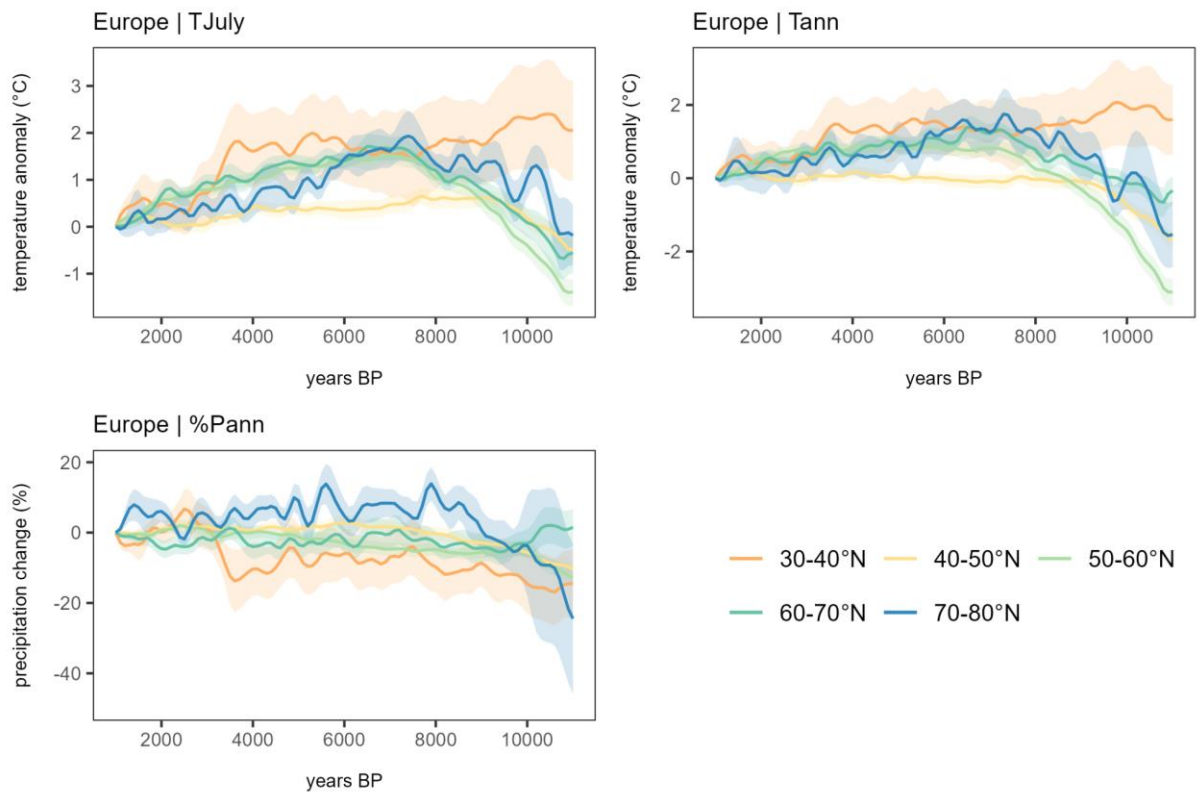
Figure A4: Western North American latitudinal mean curves with shaded standard errors for T_{July}, T_{ann}, and %P_{ann} derived from pollen-based reconstruction with WA-PLS (latitudinal bands that contain fewer than three grid cells are not shown).



612

613 **Figure A5: Eastern North American latitudinal mean curves with shaded standard errors for T_{July},**
 614 **T_{ann}, and %P_{ann} derived from pollen-based reconstruction with WA-PLS (latitudinal bands that**
 615 **contain fewer than three grid cells are not shown).**

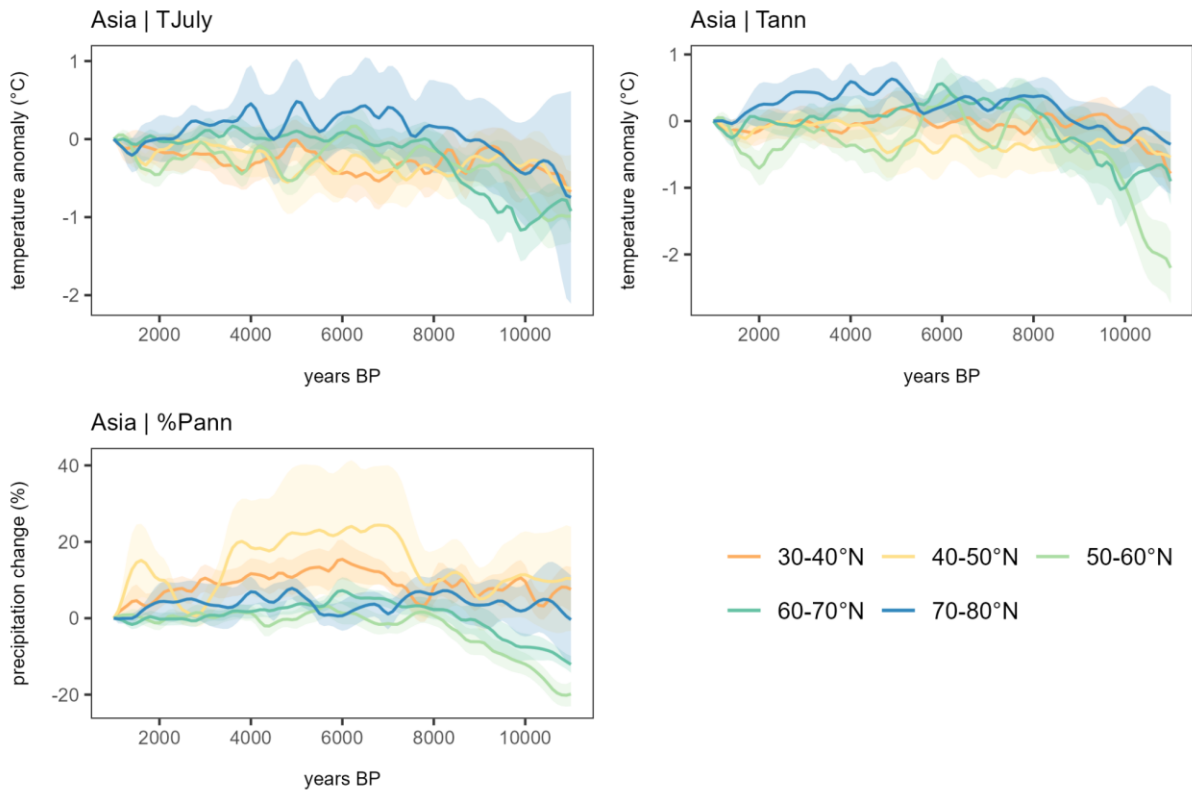
616



617

618 **Figure A6: European latitudinal mean curves with shaded standard errors for T_{July} , T_{ann} ,**
 619 **and $\%P_{ann}$ derived from pollen-based reconstruction with WA-PLS (latitudinal bands that contain**
 620 **fewer than three grid cells are not shown).**

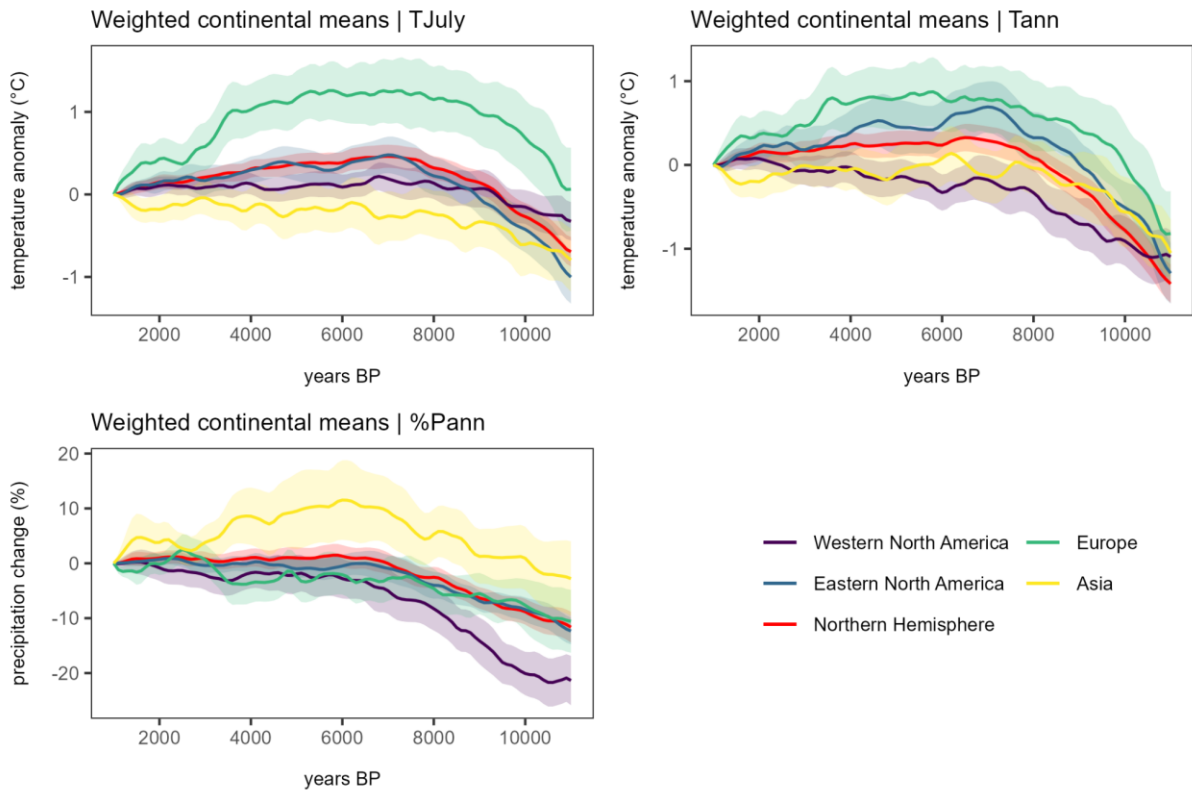
621



622

623 **Figure A7: Asian latitudinal mean curves with shaded standard errors for T_{July} , T_{ann} , and $\%P_{ann}$**
 624 **derived from pollen-based reconstruction with WA-PLS (latitudinal bands that contain fewer than**
 625 **three grid cells are not shown).**

626



627

628 **Figure A8: Weighted continental means with shaded standard errors for T_{July} , T_{ann} , and $\%P_{ann}$**
 629 **derived from pollen-based reconstruction with WA-PLS.**

630

631

632

633

634

635

636

637

638

639

640

641

642

643

644 **Table A2.** Significance values for zonal linear trends derived from a Monte-Carlo test comparison for
 645 mean July temperatures (T_{July}).

		30-40°N	40-50°N	50-60°N	60-70°N	70-80°N
Western North America	30-40°N		$p < 0.01$	$p < 0.01$	$p < 0.01$	$p < 0.01$
	40-50°N	$p < 0.01$		$p < 0.01$	$p < 0.01$	$p < 0.01$
	50-60°N	$p < 0.01$	$p < 0.01$		$p < 0.01$	$p < 0.01$
	60-70°N	$p < 0.01$	$p < 0.01$	$p < 0.01$		$p < 0.01$
	70-80°N	$p < 0.01$	$p < 0.01$	$p < 0.01$	$p < 0.01$	
Eastern North America	30-40°N		$p < 0.01$	$p < 0.01$	$p < 0.01$	$p < 0.01$
	40-50°N	$p < 0.01$		$p < 0.01$	$p < 0.01$	$p < 0.01$
	50-60°N	$p < 0.01$	$p < 0.01$		$p < 0.01$	$p < 0.01$
	60-70°N	$p < 0.01$	$p < 0.01$	$p < 0.01$		$p < 0.01$
	70-80°N	$p < 0.01$	$p < 0.01$	$p < 0.01$	$p < 0.01$	
Europe	30-40°N		$p < 0.01$	$p < 0.01$	$p < 0.01$	$p < 0.01$
	40-50°N	$p < 0.01$		$p < 0.01$	$p < 0.01$	$p < 0.01$
	50-60°N	$p < 0.01$	$p < 0.01$		$p < 0.01$	$p < 0.01$
	60-70°N	$p < 0.01$	$p < 0.01$	$p < 0.01$		$p < 0.01$
	70-80°N	$p < 0.01$	$p < 0.01$	$p < 0.01$	$p < 0.01$	
Asia	30-40°N		$p < 0.01$	$p < 0.01$	$p < 0.01$	$p < 0.01$
	40-50°N	$p < 0.01$		$p < 0.01$	$p < 0.01$	$p < 0.01$
	50-60°N	$p < 0.01$	$p < 0.01$		$p < 0.01$	$p < 0.01$
	60-70°N	$p < 0.01$	$p < 0.01$	$p < 0.01$		$p < 0.01$
	70-80°N	$p < 0.01$	$p < 0.01$	$p < 0.01$	$p < 0.01$	

647 **Table A3.** Significance values for zonal linear trends derived from a Monte-Carlo test comparison for
 648 mean annual temperatures (T_{ann}).

		30-40°N	40-50°N	50-60°N	60-70°N	70-80°N
Western North America	30-40°N		$p < 0.01$	$p < 0.01$	$p < 0.01$	$p < 0.01$
	40-50°N	$p < 0.01$		$p < 0.01$	$p < 0.01$	$p < 0.01$
	50-60°N	$p < 0.01$	$p < 0.01$		$p < 0.01$	$p < 0.01$
	60-70°N	$p < 0.01$	$p < 0.01$	$p < 0.01$		$p < 0.01$
	70-80°N	$p < 0.01$	$p < 0.01$	$p < 0.01$	$p < 0.01$	
Eastern North America	30-40°N		$p < 0.01$	$p < 0.01$	$p < 0.01$	$p < 0.01$
	40-50°N	$p < 0.01$		$p < 0.01$	$p < 0.01$	$p < 0.01$
	50-60°N	$p < 0.01$	$p < 0.01$		$p < 0.01$	$p < 0.01$
	60-70°N	$p < 0.01$	$p < 0.01$	$p < 0.01$		$p < 0.01$
	70-80°N	$p < 0.01$	$p < 0.01$	$p < 0.01$	$p < 0.01$	
Europe	30-40°N		$p < 0.01$	$p < 0.01$	$p < 0.01$	$p < 0.01$
	40-50°N	$p < 0.01$		$p < 0.01$	$p < 0.01$	$p < 0.01$
	50-60°N	$p < 0.01$	$p < 0.01$		$p < 0.01$	$p < 0.01$
	60-70°N	$p < 0.01$	$p < 0.01$	$p < 0.01$		$p < 0.01$
	70-80°N	$p < 0.01$	$p < 0.01$	$p < 0.01$	$p < 0.01$	
Asia	30-40°N		$p < 0.01$	$p < 0.01$	$p < 0.01$	$p < 0.01$
	40-50°N	$p < 0.01$		$p < 0.01$	$p < 0.01$	$p < 0.01$
	50-60°N	$p < 0.01$	$p < 0.01$		$p < 0.01$	$p < 0.01$
	60-70°N	$p < 0.01$	$p < 0.01$	$p < 0.01$		$p < 0.01$
	70-80°N	$p < 0.01$	$p < 0.01$	$p < 0.01$	$p < 0.01$	

650 **Table A4.** Significance values for zonal linear trends derived from a Monte-Carlo test comparison for
 651 annual precipitation (P_{ann}).

		30-40°N	40-50°N	50-60°N	60-70°N	70-80°N
Western North America	30-40°N		$p < 0.01$	$p < 0.01$	$p < 0.01$	$p < 0.01$
	40-50°N	$p < 0.01$		$p < 0.01$	$p < 0.01$	$p < 0.01$
	50-60°N	$p < 0.01$	$p < 0.01$		$p < 0.01$	$p < 0.01$
	60-70°N	$p < 0.01$	$p < 0.01$	$p < 0.01$		$p < 0.01$
	70-80°N	0.06	$p < 0.01$	$p < 0.01$	$p < 0.01$	
Eastern North America	30-40°N		$p < 0.01$	$p < 0.01$	$p < 0.01$	$p < 0.01$
	40-50°N	$p < 0.01$		$p < 0.01$	$p < 0.01$	$p < 0.01$
	50-60°N	$p < 0.01$	$p < 0.01$		$p < 0.01$	$p < 0.01$
	60-70°N	$p < 0.01$	$p < 0.01$	$p < 0.01$		$p < 0.01$
	70-80°N	$p < 0.01$	$p < 0.01$	$p < 0.01$	$p < 0.01$	
Europe	30-40°N		$p < 0.01$	$p < 0.01$	$p < 0.01$	$p < 0.01$
	40-50°N	$p < 0.01$		$p < 0.01$	$p < 0.01$	$p < 0.01$
	50-60°N	$p < 0.01$	$p < 0.01$		$p < 0.01$	$p < 0.01$
	60-70°N	$p < 0.01$	$p < 0.01$	$p < 0.01$		$p < 0.01$
	70-80°N	$p < 0.01$	$p < 0.01$	$p < 0.01$	$p < 0.01$	
Asia	30-40°N		0.08	$p < 0.01$	$p < 0.01$	0.76
	40-50°N	0.02		$p < 0.01$	$p < 0.01$	$p < 0.01$
	50-60°N	$p < 0.01$	$p < 0.01$		$p < 0.01$	$p < 0.01$
	60-70°N	$p < 0.01$	$p < 0.01$	$p < 0.01$		$p < 0.01$
	70-80°N	0.39	0.02	$p < 0.01$	$p < 0.01$	

652

653 **Table A5.** Significance values for continental means linear trends derived from a Monte-Carlo test
 654 comparison.

	Western North America	Eastern North America	Europe	Asia
T_{July}	Western North America		p < 0.01	p < 0.01
	Eastern North America	p < 0.01	p < 0.01	p < 0.01
	Europe	p < 0.01	p < 0.01	p < 0.01
	Asia	p < 0.01	p < 0.01	p < 0.01
T_{ann}	Western North America		p < 0.01	p < 0.01
	Eastern North America	p < 0.01	p < 0.01	p < 0.01
	Europe	p < 0.01	p < 0.01	0.08
	Asia	p < 0.01	p < 0.01	0.9
P_{ann}	Western North America		p < 0.01	p < 0.01
	Eastern North America	p < 0.01	p < 0.01	p < 0.01
	Europe	p < 0.01	p < 0.01	p < 0.01
	Asia	p < 0.01	p < 0.01	p < 0.01

655

656 **Table A6.** Significance values for continental means compared to the Northern Hemispheric mean
 657 derived from a Monte-Carlo test comparison.

	Western North America	Eastern North America	Europe	Asia
T_{July}	p < 0.01	p < 0.01	p < 0.01	p < 0.01
T_{ann}	p < 0.01	p < 0.01	p < 0.01	p < 0.01
P_{ann}	p < 0.01	p < 0.01	p < 0.01	p < 0.01

658

659 **References**

- 660 Andreev, A., Tarasov, P., Schwamborn, G., Ilyashuk, B., Ilyashuk, E., Bobrov, A., Klimanov, V., Rachold,
661 V., and Hubberten, H.-W.: Holocene paleoenvironmental records from Nikolay Lake, Lena River Delta,
662 Arctic Russia, *Palaeogeogr., Palaeoclim., Palaeoecol.*, 209, 197–217,
663 <https://doi.org/10.1016/j.palaeo.2004.02.010>, 2004.
- 664 Bader, J., Jungclaus, J., Krivova, N., Lorenz, S., Maycock, A., Raddatz, T., Schmidt, H., Toohey, M.,
665 Wu, C.-J., and Claussen, M.: Global temperature modes shed light on the Holocene temperature
666 conundrum, *Nat. Commun.*, 11, 4726, <https://doi.org/10.1038/s41467-020-18478-6>, 2020.
- 667 Bakker, P., Rogozhina, I., Merkel, U., and Prange, M.: Hypersensitivity of glacial summer temperatures
668 in Siberia, *Clim. Past*, 16, 371–386, <https://doi.org/10.5194/cp-16-371-2020>, 2020.
- 669 Birks, H. J. B., Heiri, O., Seppä, H., and Bjune, A. E.: Strengths and Weaknesses of Quantitative Climate
670 Reconstructions Based on Late-Quaternary, *Open Ecol. J.*, 3,
671 <http://dx.doi.org/10.2174/1874213001003020068>, 2010.
- 672 Birks, H. J. B. and Simpson, G. L.: ‘Diatoms and pH reconstruction’ (1990) revisited, *J. Paleolimnol.*, 49,
673 363–371, <https://doi.org/10.1007/s10933-013-9697-7>, 2013.
- 674 Blaauw, M. and Christen, J. A.: Flexible paleoclimate age-depth models using an autoregressive gamma
675 process, *Bayesian Anal.*, 6, 457–474, <https://doi.org/10.1214/11-BA618>, 2011.
- 676 Bova, S., Rosenthal, Y., Liu, Z., Godad, S. P., and Yan, M.: Seasonal origin of the thermal maxima at
677 the Holocene and the last interglacial, *Nature*, 589, 548–553, [https://doi.org/10.1038/s41586-020-](https://doi.org/10.1038/s41586-020-03155-x)
678 03155-x, 2021.
- 679 Brierley, C. M., Zhao, A., Harrison, S. P., Braconnot, P., Williams, C. J. R., Thornalley, D. J. R., Shi, X.,
680 Peterschmitt, J.-Y., Ohgaito, R., Kaufman, D. S., Kageyama, M., Hargreaves, J. C., Erb, M. P., Emile-
681 Geay, J., D’Agostino, R., Chandan, D., Carré, M., Bartlein, P. J., Zheng, W., Zhang, Z., Zhang, Q., Yang,
682 H., Volodin, E. M., Tomas, R. A., Routson, C., Peltier, W. R., Otto-Bliesner, B., Morozova, P. A., McKay,
683 N. P., Lohmann, G., Legrande, A. N., Guo, C., Cao, J., Brady, E., Annan, J. D., and Abe-Ouchi, A.:
684 Large-scale features and evaluation of the PMIP4-CMIP6 midHolocene simulations, *Clim. Past*, 16,
685 1847–1872, <https://doi.org/10.5194/cp-16-1847-2020>, 2020.
- 686 Brodzik, M. J., Billingsley, B., Haran, T., Raup, B., and Savoie, M. H.: EASE-Grid 2.0: Incremental but
687 Significant Improvements for Earth-Gridded Data Sets, *IJGI*, 1, 32–45,
688 <https://doi.org/10.3390/ijgi1010032>, 2012.
- 689 Cao, X., Ni, J., Herzschuh, U., Wang, Y., and Zhao, Y.: A late Quaternary pollen dataset from eastern
690 continental Asia for vegetation and climate reconstructions: Set up and evaluation, *Rev. Palaeobot.*
691 *Palynol.*, 194, 21–37, <https://doi.org/10.1016/j.revpalbo.2013.02.003>, 2013.

692 Cao, X., Herzschuh, U., Telford, R. J., and Ni, J.: A modern pollen–climate dataset from China and
693 Mongolia: Assessing its potential for climate reconstruction, *Rev. Palaeobot. Palynol.*, 211, 87–96,
694 <https://doi.org/10.1016/j.revpalbo.2014.08.007>, 2014.

695 Cao, X., Tian, F., Dallmeyer, A., and Herzschuh, U.: Northern Hemisphere biome changes (>30°N) since
696 40 cal ka BP and their driving factors inferred from model-data comparisons, *Quat. Sci. Rev.*, 220, 291–
697 309, <https://doi.org/10.1016/j.quascirev.2019.07.034>, 2019.

698 Cao, X., Tian, F., Telford, R. J., Ni, J., Xu, Q., Chen, F., Liu, X., Stebich, M., Zhao, Y., and Herzschuh,
699 U.: Impacts of the spatial extent of pollen-climate calibration-set on the absolute values, range and
700 trends of reconstructed Holocene precipitation, *Quat. Sci. Rev.*, 178, 37–53,
701 <https://doi.org/10.1016/j.quascirev.2017.10.030>, 2017.

702 Cartapanis, O., Jonkers, L., Moffa-Sanchez, P., Jaccard, S. L., and de Vernal, A.: Complex spatio-
703 temporal structure of the Holocene Thermal Maximum, *Nat Commun*, 13, 5662,
704 <https://doi.org/10.1038/s41467-022-33362-1>, 2022.

705 Chang, E. K. M., Lee, S., and Swanson, K. L.: Storm Track Dynamics, *J. Clim.*, 15, 2163–2183,
706 [https://doi.org/10.1175/1520-0442\(2002\)015<02163:STD>2.0.CO;2](https://doi.org/10.1175/1520-0442(2002)015<02163:STD>2.0.CO;2), 2002.

707 Chen, F., Xu, Q., Chen, J., Birks, H. J. B., Liu, J., Zhang, S., Jin, L., An, C., Telford, R. J., Cao, X., Wang,
708 Z., Zhang, X., Selvaraj, K., Lu, H., Li, Y., Zheng, Z., Wang, H., Zhou, A., Dong, G., Zhang, J., Huang,
709 X., Bloemendal, J., and Rao, Z.: East Asian summer monsoon precipitation variability since the last
710 deglaciation, *Sci. Rep.*, 5, 11186, <https://doi.org/10.1038/srep11186>, 2015.

711 Chen, F., Chen, J., Huang, W., Chen, S., Huang, X., Jin, L., Jia, J., Zhang, X., An, C., Zhang, J., Zhao,
712 Y., Yu, Z., Zhang, R., Liu, J., Zhou, A., and Feng, S.: Westerlies Asia and monsoonal Asia:
713 Spatiotemporal differences in climate change and possible mechanisms on decadal to sub-orbital
714 timescales, *Earth Sci. Rev.*, 192, 337–354, <https://doi.org/10.1016/j.earscirev.2019.03.005>, 2019.

715 Chevalier, M., Davis, B. A. S., Heiri, O., Seppä, H., Chase, B. M., Gajewski, K., Lacourse, T., Telford,
716 R. J., Finsinger, W., Guiot, J., Kühl, N., Maezumi, S. Y., Tipton, J. R., Carter, V. A., Brussel, T., Phelps,
717 L. N., Dawson, A., Zanon, M., Vallé, F., Nolan, C., Mauri, A., de Vernal, A., Izumi, K., Holmström, L.,
718 Marsicek, J., Goring, S., Sommer, P. S., Chaput, M., and Kupriyanov, D.: Pollen-based climate
719 reconstruction techniques for late Quaternary studies, *Earth Sci. Rev.*, 210, 103384,
720 <https://doi.org/10.1016/j.earscirev.2020.103384>, 2020.

721 Chouinard, C. and Mareschal, J.-C.: Ground surface temperature history in southern Canada:
722 Temperatures at the base of the Laurentide ice sheet and during the Holocene, *Earth Planet. Sci. Lett.*,
723 277, 280–289, <https://doi.org/10.1016/j.epsl.2008.10.026>, 2009.

724 Cleator, S. F., Harrison, S. P., Nichols, N. K., Prentice, I. C., and Roulstone, I.: A new multivariable
725 benchmark for Last Glacial Maximum climate simulations, *Clim. Past*, 16, 699–712,
726 <https://doi.org/10.5194/cp-16-699-2020>, 2020.

727 Dallmeyer, A., Claussen, M., Lorenz, S. J., Sigl, M., Toohey, M., and Herzschuh, U.: Holocene
728 vegetation transitions and their climatic drivers in MPI-ESM1.2, *Clim. Past*, 17, 2481–2513,
729 <https://doi.org/10.5194/cp-17-2481-2021>, 2021.

730 Dallmeyer, A., Kleinen, T., Claussen, M., Weitzel, N., Cao, X., and Herzschuh, U.: The deglacial forest
731 conundrum, *Nat Commun*, 13, 6035, <https://doi.org/10.1038/s41467-022-33646-6>, 2022.

732 Davis, B. A. S., Brewer, S., Stevenson, A. C., and Guiot, J.: The temperature of Europe during the
733 Holocene reconstructed from pollen data, *Quat. Sci. Rev.*, 22, 1701–1716,
734 [https://doi.org/10.1016/S0277-3791\(03\)00173-2](https://doi.org/10.1016/S0277-3791(03)00173-2), 2003.

735 Davis, B. A. S., Chevalier, M., Sommer, P., Carter, V. A., Finsinger, W., Mauri, A., Phelps, L. N., Zanon,
736 M., Abegglen, R., Åkesson, C. M., Alba-Sánchez, F., Anderson, R. S., Antipina, T. G., Atanassova, J.
737 R., Beer, R., Belyanina, N. I., Blyakharchuk, T. A., Borisova, O. K., Bozilova, E., Bukreeva, G., Bunting,
738 M. J., Clò, E., Colombaroli, D., Combourieu-Nebout, N., Desprat, S., Di Rita, F., Djamali, M., Edwards,
739 K. J., Fall, P. L., Feurdean, A., Fletcher, W., Florenzano, A., Furlanetto, G., Gaceur, E., Galimov, A. T.,
740 Gałka, M., García-Moreiras, I., Giesecke, T., Grindean, R., Guido, M. A., Gvozdeva, I. G., Herzschuh,
741 U., Hjelle, K. L., Ivanov, S., Jahns, S., Jankovska, V., Jiménez-Moreno, G., Karpińska-Kołaczek, M.,
742 Kitaba, I., Kołaczek, P., Lapteva, E. G., Latałowa, M., Lebreton, V., Leroy, S., Leydet, M., Lopatina, D.
743 A., López-Sáez, J. A., Lotter, A. F., Magri, D., Marinova, E., Matthias, I., Mavridou, A., Mercuri, A. M.,
744 Mesa-Fernández, J. M., Mikishin, Y. A., Milecka, K., Montanari, C., Morales-Molino, C., Mrotzek, A.,
745 Muñoz Sobrino, C., Naidina, O. D., Nakagawa, T., Nielsen, A. B., Novenko, E. Y., Panajiotidis, S.,
746 Panova, N. K., Papadopoulou, M., Pardoe, H. S., Pędziszewska, A., Petrenko, T. I., Ramos-Román, M.
747 J., Ravazzi, C., Rösch, M., Ryabogina, N., Sabariego Ruiz, S., Salonen, J. S., Sapelko, T. V., Schofield,
748 J. E., Seppä, H., Shumilovskikh, L., Stivrins, N., Stojakowits, P., Svobodova Svitavska, H., Święta-
749 Musznicka, J., Tantau, I., Tinner, W., Tobolski, K., Tonkov, S., Tsakiridou, M., et al.: The Eurasian
750 Modern Pollen Database (EMPD), version 2, *Earth Syst. Sci. Data*, 12, 2423–2445,
751 <https://doi.org/10.5194/essd-12-2423-2020>, 2020.

752 Dugerdil, L., Joannin, S., Peyron, O., Jouffroy-Bapicot, I., Vannière, B., Boldgiv, B., Unkelbach, J.,
753 Behling, H., and Ménot, G.: Climate reconstructions based on GDGT and pollen surface datasets from
754 Mongolia and Baikal area: calibrations and applicability to extremely cold–dry environments over the
755 Late Holocene, *Clim. Past*, 17, 1199–1226, <https://doi.org/10.5194/cp-17-1199-2021>, 2021.

756 Fick, S. E. and Hijmans, R. J.: WorldClim 2: new 1-km spatial resolution climate surfaces for global land
757 areas, *Int. J. Climatol.*, 37, 4302–4315, <https://doi.org/10.1002/joc.5086>, 2017.

758 Grimm, E. C., Lozano-García, S., Behling, H., and Markgraf, V.: Chapter 19 - Holocene Vegetation and
759 Climate Variability in the Americas, in: *Interhemispheric Climate Linkages*, edited by: Markgraf, V.,
760 Academic Press, San Diego, 325–370, <https://doi.org/10.1016/B978-012472670-3/50022-7>, 2001.

761 Harrell, F. E. and Dupont, C.: Hmisc: Harrell Miscellaneous, R package version 5.0-1, [https://cran.r-](https://cran.r-project.org/web/packages/Hmisc)
762 [project.org/web/packages/Hmisc](https://cran.r-project.org/web/packages/Hmisc), 2023.

763 Harrison, S. P., Kutzbach, J. E., Liu, Z., Bartlein, P. J., Otto-Bliesner, B., Muhs, D., Prentice, I. C., and
764 Thompson, R. S.: Mid-Holocene climates of the Americas: a dynamical response to changed seasonality,
765 *Clim. Dyn.*, 20, 663–688, <https://doi.org/10.1007/s00382-002-0300-6>, 2003.

766 Herzsuh, U.: Legacy of the Last Glacial on the present-day distribution of deciduous versus evergreen
767 boreal forests, *Global Ecology and Biogeography*, 29, 198–206, <https://doi.org/10.1111/geb.13018>,
768 2020.

769 Herzsuh, U., Tarasov, P., Wünnemann, B., and Hartmann, K.: Holocene vegetation and climate of
770 the Alashan Plateau, NW China, reconstructed from pollen data, *Palaeogeogr. Palaeoclimatol.*
771 *Palaeoecol.*, 211, 1–17, <https://doi.org/10.1016/j.palaeo.2004.04.001>, 2004.

772 Herzsuh, U., Birks, H. J. B., Laepple, T., Andreev, A., Melles, M., and Brigham-Grette, J.: Glacial
773 legacies on interglacial vegetation at the Pliocene-Pleistocene transition in NE Asia, *Nat Commun*, 7,
774 11967, <https://doi.org/10.1038/ncomms11967>, 2016.

775 Herzsuh, U., Cao, X., Laepple, T., Dallmeyer, A., Telford, R. J., Ni, J., Chen, F., Kong, Z., Liu, G., Liu,
776 K.-B., Liu, X., Stebich, M., Tang, L., Tian, F., Wang, Y., Wischnewski, J., Xu, Q., Yan, S., Yang, Z., Yu,
777 G., Zhang, Y., Zhao, Y., and Zheng, Z.: Position and orientation of the westerly jet determined Holocene
778 rainfall patterns in China, *Nat. Commun.*, 10, 2376, <https://doi.org/10.1038/s41467-019-09866-8>, 2019.

779 Herzsuh, U., Böhmer, T., Li, C., and Cao, X.: Northern Hemisphere temperature and precipitation
780 reconstruction from taxonomically harmonized pollen data set with revised chronologies using WA-PLS
781 and MAT (LegacyClimate 1.0), *PANGAEA*, <https://doi.org/10.1594/PANGAEA.930512>, 2023.

782 Herzsuh, U., Böhmer, T., Li, C., Chevalier, M., Dallmeyer, A., Cao, X., Bigelow, N. H., Nazarova, L.,
783 Novenko, E. Y., Park, J., Peyron, O., Rudaya, N. A., Schlütz, F., Shumilovskikh, L. S., Tarasov, P. E.,
784 Wang, Y., Wen, R., Xu, Q., and Zheng, Z.: LegacyClimate 1.0: A dataset of pollen-based climate
785 reconstructions from 2594 Northern Hemisphere sites covering the last 30 ka and beyond, *Earth Syst.*
786 *Sci. Data*, 1–29, <https://doi.org/10.5194/essd-2022-38>, 2022a.

787 Herzsuh, U., Li, C., Böhmer, T., Postl, A. K., Heim, B., Andreev, A. A., Cao, X., Wiczorek, M., and
788 Ni, J.: LegacyPollen 1.0: a taxonomically harmonized global late Quaternary pollen dataset of 2831
789 records with standardized chronologies, *Earth Syst. Sci. Data*, 14, 3213–3227,
790 <https://doi.org/10.5194/essd-14-3213-2022>, 2022b.

791 Hijmans, R. J., van Etten, J., Sumner, M., Cheng, J., Baston, D., Bevan, A., Bivand, R., Busetto, L.,
792 Canty, M., Fasoli, B., Forrest, D., Ghosh, A., Golicher, D., Gray, J., Greenberg, J. A., Hiemstra, P.,
793 Hingee, K., Ilich, A., Institute for Mathematics Applied Geosciences, Karney, C., Mattiuzzi, M., Mosher,
794 S., Naimi, B., Nowosad, J., Pebesma, E., Lamigueiro, O. P., Racine, E. B., Rowlingson, B., Shortridge,
795 A., Venables, B., and Wueest, R.: Raster: Geographic Data Analysis and Modeling, R package version
796 3.5-11, <https://cran.r-project.org/web/packages/raster>, 2021.

797 Jin, L., Chen, F., Morrill, C., Otto-Bliesner, B. L., and Rosenbloom, N.: Causes of early Holocene
798 desertification in arid central Asia, *Clim. Dyn.*, 38, 1577–1591, [https://doi.org/10.1007/s00382-011-](https://doi.org/10.1007/s00382-011-1086-1)
799 1086-1, 2012.

800 Juggins, S.: Quantitative reconstructions in palaeolimnology: new paradigm or sick science?, *Quat. Sci.*
801 *Rev.*, 64, 20–32, <https://doi.org/10.1016/j.quascirev.2012.12.014>, 2013.

802 Kaufman, D., McKay, N., Routson, C., Erb, M., Davis, B., Heiri, O., Jaccard, S., Tierney, J., Dätwyler,
803 C., Axford, Y., Brussel, T., Cartapanis, O., Chase, B., Dawson, A., de Vernal, A., Engels, S., Jonkers,
804 L., Marsicek, J., Moffa-Sánchez, P., Morrill, C., Orsi, A., Rehfeld, K., Saunders, K., Sommer, P. S.,
805 Thomas, E., Tonello, M., Tóth, M., Vachula, R., Andreev, A., Bertrand, S., Biskaborn, B., Bringué, M.,
806 Brooks, S., Caniupán, M., Chevalier, M., Cwynar, L., Emile-Geay, J., Fegyveresi, J., Feurdean, A.,
807 Finsinger, W., Fortin, M.-C., Foster, L., Fox, M., Gajewski, K., Grosjean, M., Hausmann, S., Heinrichs,
808 M., Holmes, N., Ilyashuk, B., Ilyashuk, E., Juggins, S., Khider, D., Koinig, K., Langdon, P., Larocque-
809 Tobler, I., Li, J., Lotter, A., Luoto, T., Mackay, A., Magyar, E., Malevich, S., Mark, B., Massaferró, J.,
810 Montade, V., Nazarova, L., Novenko, E., Pařil, P., Pearson, E., Peros, M., Pienitz, R., Plóciennik, M.,
811 Porinchu, D., Potito, A., Rees, A., Reinemann, S., Roberts, S., Rolland, N., Salonen, S., Self, A., Seppä,
812 H., Shala, S., St-Jacques, J.-M., Stenni, B., Syrykh, L., Tarrats, P., Taylor, K., van den Bos, V., Velle,
813 G., Wahl, E., Walker, I., Wilmshurst, J., Zhang, E., and Zhilich, S.: A global database of Holocene
814 paleotemperature records, *Sci. Data*, 7, 115, <https://doi.org/10.1038/s41597-020-0445-3>, 2020a.

815 Kaufman, D., McKay, N., Routson, C., Erb, M., Dätwyler, C., Sommer, P. S., Heiri, O., and Davis, B.:
816 Holocene global mean surface temperature, a multi-method reconstruction approach, *Sci. Data*, 7, 201,
817 <https://doi.org/10.1038/s41597-020-0530-7>, 2020b.

818 Kaufman, D. S. and Broadman, E.: Revisiting the Holocene global temperature conundrum, *Nature*,
819 614, 425–435, <https://doi.org/10.1038/s41586-022-05536-w>, 2023.

820 Kubota, Y., Tada, R., and Kimoto, K.: Changes in East Asian summer monsoon precipitation during the
821 Holocene deduced from a freshwater flux reconstruction of the Changjiang (Yangtze River) based on
822 the oxygen isotope mass balance in the northern East China Sea, *Clim. Past*, 11, 265–281,
823 <https://doi.org/10.5194/cp-11-265-2015>, 2015.

824 Kutzbach, J. E.: Monsoon Climate of the Early Holocene: Climate Experiment with the Earth's Orbital
825 Parameters for 9000 Years Ago, *Science*, <https://doi.org/10.1126/science.214.4516.59>, 1981.

826 Ladd, M., Way, R. G., and Viau, A. E.: The impact of using different modern climate data sets in pollen-
827 based paleoclimate reconstructions of North America, *Quat. Sci. Rev.*, 112, 78–85,
828 <https://doi.org/10.1016/j.quascirev.2015.01.020>, 2015.

829 Leipe, C., Nakagawa, T., Gotanda, K., Müller, S., and Tarasov, P. E.: Late Quaternary vegetation and
830 climate dynamics at the northern limit of the East Asian summer monsoon and its regional and global-
831 scale controls, *Quat. Sci. Rev.*, 116, 57–71, <https://doi.org/10.1016/j.quascirev.2015.03.012>, 2015.

832 Li, C., Postl, A. K., Böhmer, T., Cao, X., Dolman, A. M., and Herzsuh, U.: Harmonized chronologies
833 of a global late Quaternary pollen dataset (LegacyAge 1.0), *Earth Syst. Sci. Data*, 14, 1331–1343,
834 <https://doi.org/10.5194/essd-14-1331-2022>, 2022.

835 Li, J., Wang, N., Dodson, J., Yan, H., Zhang, X., Jia, P. W., and Seppä, H.: Holocene negative coupling
836 of summer temperature and moisture availability over southeastern arid Central Asia, *Clim. Dyn.*, 55,
837 1187–1208, <https://doi.org/10.1007/s00382-020-05319-x>, 2020.

838 Liu, Z., Wen, X., Brady, E. C., Otto-Bliesner, B., Yu, G., Lu, H., Cheng, H., Wang, Y., Zheng, W., Ding,
839 Y., Edwards, R. L., Cheng, J., Liu, W., and Yang, H.: Chinese cave records and the East Asia Summer
840 Monsoon, *Quat. Sci. Rev.*, 83, 115–128, <https://doi.org/10.1016/j.quascirev.2013.10.021>, 2014a.

841 Liu, Z., Yoshimura, K., Bowen, G. J., Buening, N. H., Risi, C., Welker, J. M., and Yuan, F.: Paired
842 oxygen isotope records reveal modern North American atmospheric dynamics during the Holocene, *Nat.*
843 *Commun.*, 5, 3701, <https://doi.org/10.1038/ncomms4701>, 2014b.

844 Liu, Z., Zhu, J., Rosenthal, Y., Zhang, X., Otto-Bliesner, B. L., Timmermann, A., Smith, R. S., Lohmann,
845 G., Zheng, W., and Timm, O. E.: The Holocene temperature conundrum, *PNAS*, 111, E3501–E3505,
846 <https://doi.org/10.1073/pnas.1407229111>, 2014c.

847 Lohmann, G., Wagner, A., and Prange, M.: Resolution of the atmospheric model matters for the
848 Northern Hemisphere Mid-Holocene climate, *Dyn. Atmospheres Oceans*, 93, 101206,
849 <https://doi.org/10.1016/j.dynatmoce.2021.101206>, 2021.

850 Marcott, S. A., Shakun, J. D., Clark, P. U., and Mix, A. C.: A Reconstruction of Regional and Global
851 Temperature for the Past 11,300 Years, *Science*, <https://doi.org/10.1126/science.1228026>, 2013.

852 Marsicek, J., Shuman, B. N., Bartlein, P. J., Shafer, S. L., and Brewer, S.: Reconciling divergent trends
853 and millennial variations in Holocene temperatures, *Nature*, 554, 92–96,
854 <https://doi.org/10.1038/nature25464>, 2018.

855 Mauri, A., Davis, B. a. S., Collins, P. M., and Kaplan, J. O.: The influence of atmospheric circulation on
856 the mid-Holocene climate of Europe: a data–model comparison, *Clim. Past*, 10, 1925–1938,
857 <https://doi.org/10.5194/cp-10-1925-2014>, 2014.

858 Mauri, A., Davis, B. A. S., Collins, P. M., and Kaplan, J. O.: The climate of Europe during the Holocene:
859 a gridded pollen-based reconstruction and its multi-proxy evaluation, *Quat. Sci. Rev.*, 112, 109–127,
860 <https://doi.org/10.1016/j.quascirev.2015.01.013>, 2015.

861 McKay, N. P., Kaufman, D. S., Routson, C. C., Erb, M. P., and Zander, P. D.: The Onset and Rate of
862 Holocene Neoglacial Cooling in the Arctic, *Geophys. Res. Lett.*, 45, 12,487–12,496,
863 <https://doi.org/10.1029/2018GL079773>, 2018.

864 Melles, M., Brigham-Grette, J., Minyuk, P.S., Nowaczyk, N.R., Wennrich, V., DeConto, R.M., Anderson,
865 P.M., Andreev, A.A., Coletti, A., Cook, T.L., Haltia-Hovi, E., Kukkonen, M., Lozhkin, A.V., Rosén, P.,
866 Tarasov, P., Vogel, H., and Wagner, B.: 2.8 Million years of Arctic climate change from Lake El'gygytgyn,
867 NE Russia, *Science*, 337, 315–320, <https://www.science.org/doi/10.1126/science.1222135>, 2012.

868 Nakagawa, T., Tarasov, P. E., Nishida, K., Gotanda, K., and Yasuda, Y.: Quantitative pollen-based
869 climate reconstruction in central Japan: application to surface and Late Quaternary spectra, *Quat. Sci.*
870 *Rev.*, 21, 2099–2113, [https://doi.org/10.1016/S0277-3791\(02\)00014-8](https://doi.org/10.1016/S0277-3791(02)00014-8), 2002.

871 Nolan, C., Tipton, J., Booth, R. K., Hooten, M. B., and Jackson, S. T.: Comparing and improving methods
872 for reconstructing peatland water-table depth from testate amoebae, *Holocene*, 29, 1350–1361,
873 <https://doi.org/10.1177/0959683619846969>, 2019.

874 Osman, M. B., Tierney, J. E., Zhu, J., Tardif, R., Hakim, G. J., King, J., and Poulsen, C. J.: Globally
875 resolved surface temperatures since the Last Glacial Maximum, *Nature*, 599, 239–244,
876 <https://doi.org/10.1038/s41586-021-03984-4>, 2021.

877 R Core Team: R: A language and environment for statistical computing, R Foundation for Statistical
878 Computing, Vienna, Austria, <https://www.r-project.org/>, 2020.

879 Renssen, H., Seppä, H., Heiri, O., Roche, D. M., Goosse, H., and Fichefet, T.: The spatial and temporal
880 complexity of the Holocene thermal maximum, *Nat. Geosci.*, 2, 411–414,
881 <https://doi.org/10.1038/ngeo513>, 2009.

882 Renssen, H., Seppä, H., Crosta, X., Goosse, H., and Roche, D. M.: Global characterization of the
883 Holocene Thermal Maximum, *Quat. Sci. Rev.*, 48, 7–19,
884 <https://doi.org/10.1016/j.quascirev.2012.05.022>, 2012.

885 Reschke, M., Kunz, T., and Laepple, T.: Comparing methods for analysing time scale dependent
886 correlations in irregularly sampled time series data, *Comput. Geosci.*, 123, 65–72,
887 <https://doi.org/10.1016/j.cageo.2018.11.009>, 2019.

888 Rolandone, F., Mareschal, J.-C., and Jaupart, C.: Temperatures at the base of the Laurentide Ice Sheet
889 inferred from borehole temperature data, *Geophys. Res. Lett.*, 30,
890 <https://doi.org/10.1029/2003GL018046>, 2003.

891 Routson, C. C., McKay, N. P., Kaufman, D. S., Erb, M. P., Goosse, H., Shuman, B. N., Rodysill, J. R.,
892 and Ault, T.: Mid-latitude net precipitation decreased with Arctic warming during the Holocene, *Nature*,
893 568, 83–87, <https://doi.org/10.1038/s41586-019-1060-3>, 2019.

894 Routson, C. C., Kaufman, D. S., McKay, N. P., Erb, M. P., Arcusa, S. H., Brown, K. J., Kirby, M. E.,
895 Marsicek, J. P., Anderson, R. S., Jiménez-Moreno, G., Rodysill, J. R., Lachniet, M. S., Fritz, S. C.,
896 Bennett, J. R., Goman, M. F., Metcalfe, S. E., Galloway, J. M., Schoups, G., Wahl, D. B., Morris, J. L.,
897 Staines-Urías, F., Dawson, A., Shuman, B. N., Gavin, D. G., Munroe, J. S., and Cumming, B. F.: A
898 multiproxy database of western North American Holocene paleoclimate records, *Earth Syst. Sci. Data*,
899 13, 1613–1632, <https://doi.org/10.5194/essd-13-1613-2021>, 2021.

900 Salonen, J. S., Korpela, M., Williams, J. W., and Luoto, M.: Machine-learning based reconstructions of
901 primary and secondary climate variables from North American and European fossil pollen data, *Sci.*
902 *Rep.*, 9, 15805, <https://doi.org/10.1038/s41598-019-52293-4>, 2019.

903 Seager, R., Neelin, D., Simpson, I., Liu, H., Henderson, N., Shaw, T., Kushnir, Y., Ting, M., and Cook,
904 B.: Dynamical and Thermodynamical Causes of Large-Scale Changes in the Hydrological Cycle over
905 North America in Response to Global Warming, *J. Clim.*, 27, 7921–7948, <https://doi.org/10.1175/JCLI->
906 [D-14-00153.1](https://doi.org/10.1175/JCLI-14-00153.1), 2014.

907 Shin, S.-I., Sardeshmukh, P. D., Webb, R. S., Oglesby, R. J., and Barsugli, J. J.: Understanding the
908 Mid-Holocene Climate, *J. Clim.*, 19, 2801–2817, <https://doi.org/10.1175/JCLI3733.1>, 2006.

909 Simpson, G. L.: Analogue Methods in Palaeolimnology, in: *Tracking Environmental Change Using Lake*
910 *Sediments*, vol. 5: Data Handling and Numerical Techniques, edited by: Birks, H. J. B., Lotter, A. F.,
911 Juggins, S., and Smol, J. P., Springer Netherlands, Dordrecht, 495–522, <https://doi.org/10.1007/978->
912 [94-007-2745-8_15](https://doi.org/10.1007/978-94-007-2745-8_15), 2012.

913 Stebich, M., Rehfeld, K., Schlütz, F., Tarasov, P. E., Liu, J., and Mingram, J.: Holocene vegetation and
914 climate dynamics of NE China based on the pollen record from Sihailongwan Maar Lake, *Quat. Sci.*
915 *Rev.*, 124, 275–289, <https://doi.org/10.1016/j.quascirev.2015.07.021>, 2015.

916 Tarasov, P. E., Bezrukova, E. V., and Krivonogov, S. K.: Late Glacial and Holocene changes in
917 vegetation cover and climate in southern Siberia derived from a 15 kyr long pollen record from Lake
918 Kotokel, *Clim. Past*, 2009.

919 Tarasov, P. E., Nakagawa, T., Demske, D., Österle, H., Igarashi, Y., Kitagawa, J., Mokhova, L.,
920 Bazarova, V., Okuda, M., Gotanda, K., Miyoshi, N., Fujiki, T., Takemura, K., Yonenobu, H., and Fleck,
921 A.: Progress in the reconstruction of Quaternary climate dynamics in the Northwest Pacific: A new
922 modern analogue reference dataset and its application to the 430-kyr pollen record from Lake Biwa,
923 *Earth Sci. Rev.*, 108, 64–79, <https://doi.org/10.1016/j.earscirev.2011.06.002>, 2011.

924 Tarasov, P. E., Müller, S., Zech, M., Andreeva, D., Diekmann, B., and Leipe, C.: Last glacial vegetation
925 reconstructions in the extreme-continental eastern Asia: Potentials of pollen and n-alkane biomarker
926 analyses, *Quat. Int.*, 290–291, 253–263, <https://doi.org/10.1016/j.quaint.2012.04.007>, 2013.

927 Telford, R. J. and Birks, H. J. B.: A novel method for assessing the statistical significance of quantitative
928 reconstructions inferred from biotic assemblages, *Quat. Sci. Rev.*, 30, 1272–1278,
929 <https://doi.org/10.1016/j.quascirev.2011.03.002>, 2011.

930 ter Braak, C. J. F. and Juggins, S.: Weighted averaging partial least squares regression (WA-PLS): an
931 improved method for reconstructing environmental variables from species assemblages, *Hydrobiologia*,
932 269, 485–502, <https://doi.org/10.1007/BF00028046>, 1993.

933 Trenberth, K. E.: Changes in precipitation with climate change, *Clim. Res.*, 47, 123–138,
934 <https://doi.org/10.3354/cr00953>, 2011.

935 Wang, N., Jiang, D., and Lang, X.: Mechanisms for Spatially Inhomogeneous Changes in East Asian
936 Summer Monsoon Precipitation during the Mid-Holocene, *J. Clim.*, 33, 2945–2965,
937 <https://doi.org/10.1175/JCLI-D-19-0565.1>, 2020.

938 Wang, Y., Liu, X., and Herzschuh, U.: Asynchronous evolution of the Indian and East Asian Summer
939 Monsoon indicated by Holocene moisture patterns in monsoonal central Asia, *Earth Sci. Rev.*, 103, 135–
940 153, <https://doi.org/10.1016/j.earscirev.2010.09.004>, 2010.

941 Wang, Y., Bekeschus, B., Handorf, D., Liu, X., Dallmeyer, A., and Herzschuh, U.: Coherent tropical-
942 subtropical Holocene see-saw moisture patterns in the Eastern Hemisphere monsoon systems, *Quat.*
943 *Sci. Rev.*, 169, 231–242, <https://doi.org/10.1016/j.quascirev.2017.06.006>, 2017.

944 Whitmore, J., Gajewski, K., Sawada, M., Williams, J. W., Shuman, B., Bartlein, P. J., Minckley, T., Viau,
945 A. E., Webb, T., Shafer, S., Anderson, P., and Brubaker, L.: Modern pollen data from North America
946 and Greenland for multi-scale paleoenvironmental applications, *Quat. Sci. Rev.*, 24, 1828–1848,
947 <https://doi.org/10.1016/j.quascirev.2005.03.005>, 2005.

948 Williams, J. W., Grimm, E. C., Blois, J. L., Charles, D. F., Davis, E. B., Goring, S. J., Graham, R. W.,
949 Smith, A. J., Anderson, M., Arroyo-Cabrales, J., Ashworth, A. C., Betancourt, J. L., Bills, B. W., Booth,
950 R. K., Buckland, P. I., Curry, B. B., Giesecke, T., Jackson, S. T., Latorre, C., Nichols, J., Purdum, T.,
951 Roth, R. E., Stryker, M., and Takahara, H.: The Neotoma Paleoecology Database, a multiproxy,
952 international, community-curated data resource, *Quat. Res.*, 89, 156–177,
953 <https://doi.org/10.1017/qua.2017.105>, 2018.

954 Williams, J. W., Webb III, T., Richard, P. H., and Newby, P.: Late Quaternary biomes of Canada and the
955 eastern United States, *J. Biogeogr.*, 27, 585–607, <https://doi.org/10.1046/j.1365-2699.2000.00428.x>,
956 2000.

- 957 Xu, C., Yan, M., Ning, L., and Liu, J.: Summer Westerly Jet in Northern Hemisphere during the Mid-
958 Holocene: A Multi-Model Study, *Atmos.*, 11, 1193, <https://doi.org/10.3390/atmos11111193>, 2020.
- 959 Zanon, M., Davis, B. A. S., Marquer, L., Brewer, S., and Kaplan, J. O.: European Forest Cover During
960 the Past 12,000 Years: A Palynological Reconstruction Based on Modern Analogs and Remote Sensing,
961 *Front. Plant Sci.*, 9, 253, <https://doi.org/10.3389/fpls.2018.00253>, 2018.
- 962 Zhang, J., Chen, F., Holmes, J. A., Li, H., Guo, X., Wang, J., Li, S., Lü, Y., Zhao, Y., and Qiang, M.:
963 Holocene monsoon climate documented by oxygen and carbon isotopes from lake sediments and peat
964 bogs in China: a review and synthesis, *Quat. Sci. Rev.*, 30, 1973–1987,
965 <https://doi.org/10.1016/j.quascirev.2011.04.023>, 2011.
- 966 Zhang, Y., Renssen, H., and Seppä, H.: Effects of melting ice sheets and orbital forcing on the early
967 Holocene warming in the extratropical Northern Hemisphere, *Clim. Past*, 12, 1119–1135,
968 <https://doi.org/10.5194/cp-12-1119-2016>, 2016.
- 969 Zhang, Z., Liu, J., Chen, J., Chen, S., Shen, Z., Chen, J., Liu, X., Wu, D., Sheng, Y., and Chen, F.:
970 Holocene climatic optimum in the East Asian monsoon region of China defined by climatic stability, *Earth
971 Sci. Rev.*, 212, 103450, <https://doi.org/10.1016/j.earscirev.2020.103450>, 2021.
- 972 Zheng, W., Wu, B., He, J., and Yu, Y.: The East Asian Summer Monsoon at mid-Holocene: results from
973 PMIP3 simulations, *Clim. Past*, 9, 453–466, <https://doi.org/10.5194/cp-9-453-2013>, 2013.
- 974 Zhou, P., Shi, Z., Li, X., and Zhou, W.: Response of Westerly Jet Over the Northern Hemisphere to
975 Astronomical Insolation During the Holocene, *Front. Earth Sci.*, 8,
976 <https://doi.org/10.3389/feart.2020.00282>, 2020.